Effects of Wall Roughness over Forward Facing Step in Open Channel Turbulent Flow

By

S M Rifat

A Thesis submitted to the Faculty of Graduate Studies of

The University of Manitoba

in partial fulfilment of the requirements of the degree of

MASTER OF SCIENCE

Department of Mechanical Engineering

University of Manitoba

Winnipeg

ABSTRACT

An experimental investigation was performed to evaluate the effects of wall roughness on the reattachment and recovery regions over a forward facing step in an open channel turbulent flow. Detailed velocity measurements were conducted using a particle image velocimetry (PIV) system over four wall conditions: a smooth upstream and downstream wall, an upstream rough wall produced from sandpaper 36 grit and a smooth downstream wall, an upstream rough wall produced from sand grain and a smooth downstream wall, and an upstream rough surface coated with sandpaper 36 grit and a rough downstream wall coated with sandpaper 36 grit. The streamwise and wall-normal mean velocities, Reynolds stresses, turbulent kinetic energy and integral parameters were obtained and compared with previous studies. The results show that wall roughness reduced the reattachment length by as much as 29%. Moreover, roughness reduced the mean velocities in the recirculation region; however, the Reynolds stresses and turbulent kinetic energy were enhanced compared to smooth wall values. Furthermore, two-point autocorrelation function and quadrant analysis were used to investigate roughness effects on large scale coherent structures in the flow.

ACKNOWLEDGEMENT

I would like to express my sincere gratitude to my academic advisor Dr. Mark F. Tachie for his invaluable guidance and continuous support during this research.

I am very grateful for the financial support provided by the Province of Manitoba for Manitoba Graduate Scholarship and University of Manitoba for University of Manitoba Graduate Fellowship and University of Manitoba Graduate Entrance Scholarship.

Last but not the least, I would also like to acknowledge the technical support from Paul Krueger. The support and encouragement received from my colleague Ebenezer Essel is greatly appreciated. I would like to thank André L. Marchildon for helping me with the experiments. I would also like to convey my sincere thanks to all my friends especially Ebadur Rahman, Iqbal Chowdhury, Tanzeem Bin Noor, Adnan Alam Khan, Afzal Hossain Neelav and Anjum Ovi for their support and advice.

DEDICATION

This thesis is dedicated to my parents, Mr. S M Mansur and Mrs. Rokeya Begum and my brother, Mr. S M Rafiz for their love and support and for training me to be humble, hardworking and honest. I would like to dedicate this thesis to my wife, Mrs. Tamkin Rishalat Joity, for her continuous love and support throughout my stay in University of Manitoba.

TABLE OF CONTENTS

LIST OF FIGURES

LIST OF TABLES

NOMENCLATURE

English

B	logarithmic law constant
C_f	skin friction coefficient
Fr	Froude number based on upstream water depth
h	step height
H	shape factor
H_d	downstream water depth
H_r	vertical height of primary recirculation bubble
H_u	upstream water depth
k	average roughness height
k_s	equivalent sand grain roughness height
k_s^+	equivalent sand grain Reynolds number
Ku	flatness
L	length of the step
L_r	reattachment length
L_u	streamwise distance from inlet to step

L_y^u	wall-normal extent of R_{uu}
L_y^v	wall-normal extent of R_{vv}
P_k	production of turbulent kinetic energy
R_h	Reynolds number based on step height
R_θ	Reynolds number based on momentum thickness
R_{uu}	streamwise correlation function
R_{vv}	wall-normal correlation function
Sk	Skewness
$\sqrt{\overline{u'^2}}$	streamwise turbulence intensity
u'	streamwise velocity fluctuation
$\overline{u'^2}$	streamwise Reynolds normal stress
$\sqrt{\overline{v'^2}}$	wall-normal turbulence intensity
v'	wall-normal velocity fluctuation
$\overline{v'^2}$	wall-normal Reynolds normal stress
$\overline{u'v'}$	Reynolds shear stress
$\overline{u'^3}, \overline{u'^2v'}, \overline{u'v'^2}, \overline{v'^3}$	triple velocity correlations

U	local streamwise mean velocity
U^+	streamwise mean velocity normalized by friction velocity
U_e	freestream mean velocity
U_m	local maximum streamwise mean velocity
U_m*	normalized local maximum streamwise mean velocity
$U_{m@-1.5}$	maximum streamwise mean velocity at x/h = -1.5
U_τ	friction velocity
V	wall-normal mean velocity
W	width of the step
x	streamwise distance
y	wall-normal distance
y^+	wall-normal distance normalized with viscous length scale
Δx	streamwise spatial distance
Δy	wall-normal spatial distance

Greek

ΔB^+	downward-right roughness shift
δ	boundary layer thickness

δ^*	displacement thickness
Δs	local displacement vector
Δt	laser time delay
ε	dissipation
κ	von Kármán constant
η	Kolmogorov length scale
λ	Taylor microscale
Π	Coles wake parameter
ρ_p	particle density
ρ_f	fluid density
θ	momentum thickness
t_r	particle response time
μ_f	dynamic viscosity of the fluid
ν	kinematic viscosity

Acronyms

AR	aspect ratio

APG	adverse pressure gradient
BFS	backward facing step
CCD	charged coupled device
DNS	direct numerical simulation
FFS	forward facing step
IA	interrogation area
LDV	laser Doppler anemometry
LES	large eddy simulation
Nd: YAG	neodymium: Yttrium Aluminum Garnet
PIV	particle image velocimetry
ZPG	zero pressure gradient

CHAPTER 1

INTRODUCTION

1.1 Motivation

Separation and reattachment of turbulent shear flow, and its subsequent redevelopment after some streamwise distance are important research topics within the turbulent research community. Flow separation may be caused by severe adverse pressure gradient or sudden geometrical changes in the flow field. Geometry-induced flow separation and reattachment are encountered in many engineering and environmental applications. These applications include fluid-thermal devices such as combustors, gas turbines and wind turbines as well as pipe systems, water and wastewater drainage system and atmospheric flows around buildings. For fluid-thermal devices, such flow phenomena may lead to undesirable effects as structural vibration and reduced efficiency. Flow separation is also responsible for high vehicle drag which leads to a high consumption of fuel.

Due to their diverse engineering, environmental and industrial applications, the turbulence research community has invested significant efforts in advancing physical understanding of flow separation and reattachment. More specifically, both experimental and numerical studies have been performed over the past decades to understand the characteristics of separated and reattached turbulent flows. The experimental studies were performed using hotwire anemometry (HWA), laser Doppler velocimetry (LDV), acoustic Doppler velocimetry (ADV) and particle image velocimetry (PIV) (Adams and Johnston, 1988; Tachie et al., 2001; Essel et al., 2015, Essel and Tachie, 2015) while the numerical studies include those performed using direct numerical simulation (DNS) and

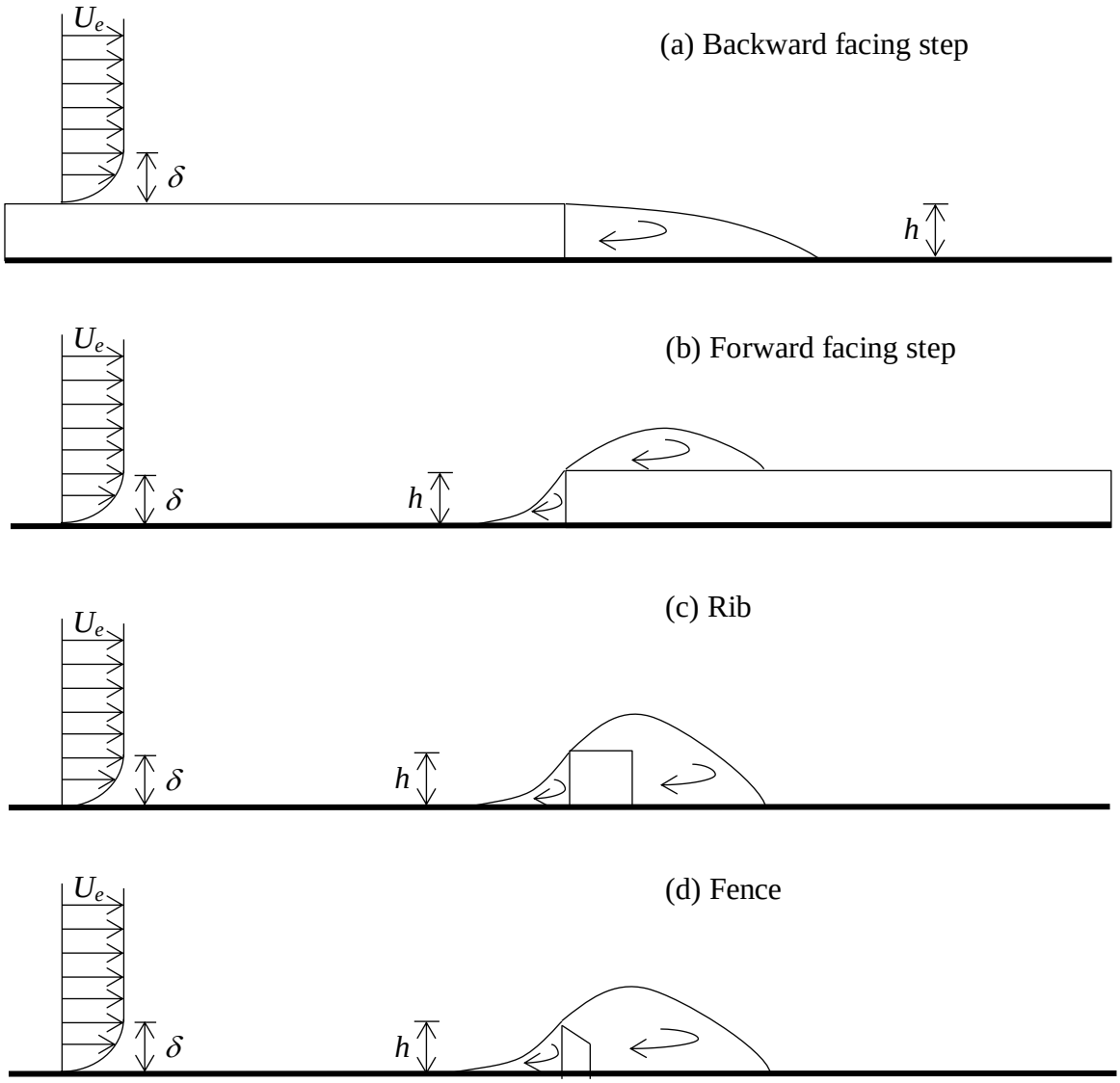

Figure 1.1: Schematic diagrams of the various geometries used to induce flow separation. Here h is the height of the step or obstacle U_e is the streamwise mean velocity, δ is the boundary layer thickness and direction of flow is indicated by arrows.

large eddy simulation (LES) (Hattori and Nagano, 2010; Barril, 2010). Figure 1.1 shows examples of the different types of configurations that have been used in previous studies to investigate the mean and turbulent characteristics of separated and reattached turbulent

shear flows. These examples include backward facing step (BFS), forward facing step (FFS), rib and fence. It can be seen from the figure that the BFS has only one separation point at the trailing edge of the step, and one reattachment point immediately downstream of the step which produces the primary recirculation region. On the contrary, the other geometries shown in the figure have two separation and two reattachment points, producing two recirculation regions before and after the obstacles.

Most of the previous studies on separated and reattached flows have been performed in wind tunnel or closed channel. However, there are numerous applications where free-surface boundary conditions are present. Such applications include water and wastewater drainage system, storm drains and irrigation channels. Unfortunately, there are only a handful of studies that investigated separated and reattached flows exposed to a free surface. Therefore, there is a need to systematically investigate the turbulent characteristics and transport phenomena in separated and reattached turbulent flow in an open channel.

Numerous investigations of separated and reattached flows have been performed on a smooth wall; however, there are only a handful studies that examine the effect of wall roughness on separated and reattached turbulent flows. Meanwhile, wall roughness is a distinct feature in many practical applications and may originate from corrosion, cavitation, sedimentation, erosion and debris deposition. For canonical turbulent boundary layers, wall roughness has been observed to enhance mixing, mass and momentum transport. Meanwhile the effects of wall roughness on the characteristics of separated and reattached flows are not well understood.

1.2 Objective and scope of research

The main objective of the present study is to investigate the effects of upstream and downstream wall roughness on the dynamics of turbulent flows over a forward facing step in an open channel.

An experimental technique was used to achieve this objective. Specifically, detailed velocity measurements were conducted over three different upstream wall conditions (a smooth wall made from a clear acrylic plate and two different rough walls produced from sandpaper 36 grit and sand grain) and two different downstream wall conditions (a smooth wall made from a clear acrylic plate and a rough wall produced from sandpaper 36 grit). A particle image velocimetry (PIV) technique was used to perform the velocity measurements. The velocity data obtained over these wall conditions were post-processed to obtain the mean velocities and turbulent quantities. In order to reveal the coherent structures embedded within the flow fields, two-point correlation and quadrant analysis were employed.

1.3 Organization of Thesis

The thesis is organized into five chapters. The salient features of a FFS and a review of previous works on separated and reattached flows over a FFS are provided in Chapter 2. Detailed description of the experimental setup including test facility, test conditions, the PIV system used for velocity measurements and detailed measurement procedure are presented in Chapter 3. Results and discussion are presented in Chapter 4. Finally, conclusions and recommendations for future work are presented in Chapter 5.

CHAPTER 2

LITERATURE REVIEW

An overview of previous experimental and numerical studies on separated and reattached turbulent flows over a forward facing step (FFS) is presented in this chapter. In order to better understand the complex characteristics of separated and reattached turbulent flows, a brief introduction of the boundary layer concept, FFS, open channel turbulent flow and rough wall turbulent boundary layer are presented before reviewing previous literature on separated and reattached turbulent flows.

2.1 Salient features of forward facing step

A schematic diagram of the salient features of turbulent flow over a FFS in an open channel and the nomenclature used in the present study are shown in Figure 2.1. A FFS of height, h is placed at a distance L_u from the inlet section of the open channel. The upstream water depth is denoted as H_u and the downstream water depth (over the FFS) is denoted as H_d. The Cartesian coordinate system adopted has the x-coordinate in the streamwise direction and the y-coordinate in the wall-normal direction. The origin of the x-coordinate is at the leading edge of the step and the origin of the y-coordinate is on top of the upstream wall of the channel.

An approach boundary layer with free stream velocity, U_e and boundary layer thickness, δ separates at a distance l_r upstream of the leading edge of the step and reattaches on to the front-face of the step at a distance h_r above the upstream wall. At the leading edge of the step, a second separation occurs and the separated shear layer reattaches onto the step after a streamwise distance, L_r. Beyond the reattachment point, the shear layer redevelops

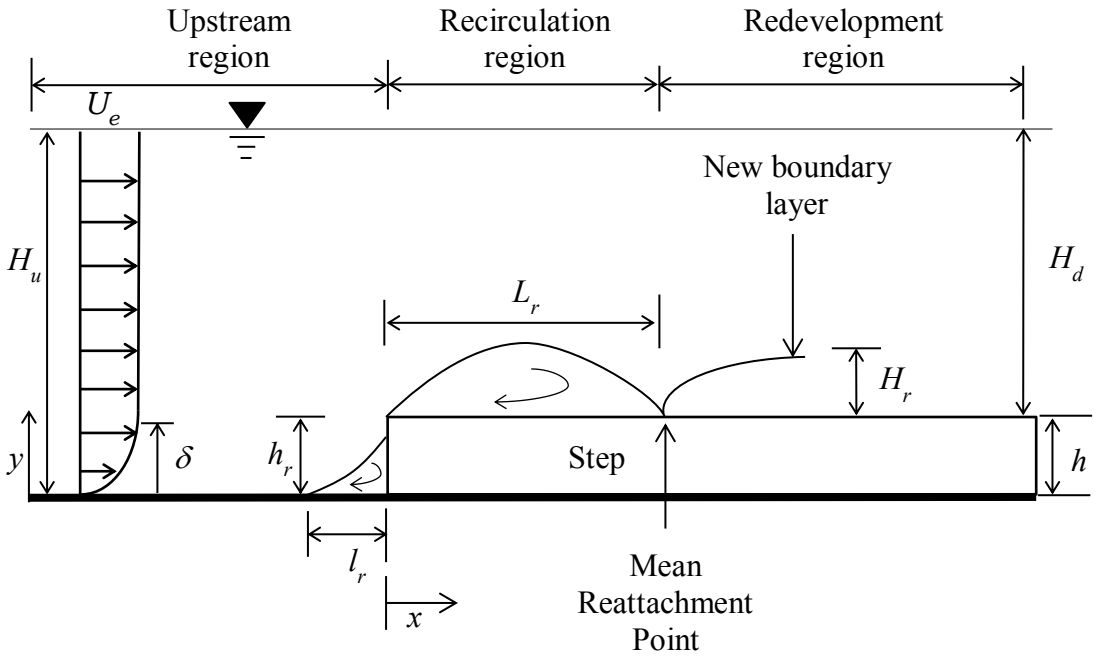

Figure 2.1: Schematic diagram of various regions of flow over a FFS.

into a new boundary layer. The recirculation bubbles formed upstream of the step and on top of the step are often referred to as the secondary and primary recirculation bubbles, respectively. The flow field can be divided into three main regions: (i) upstream region, (ii) recirculation region which spans from the leading edge to the reattachment point and (iii) recovery or redevelopment region which is the region beyond the reattachment point. The flow characteristics of these three main regions are presented in the following section.

2.1.1 Upstream, recirculation and recovery region

The upstream region is the region prior to separation and the flow characteristics in this region are similar to those of a fully developed channel flow. A boundary layer is the layer of fluid in the immediate vicinity of the wall where the effects of viscosity are significant. One important parameter of the turbulent boundary layer is the boundary layer thickness (δ) which is defined as the wall-normal distance from the wall to the location where the local streamwise mean velocity (U) is 99% of the freestream mean velocity (U_e). In addition to the boundary layer thickness, other parameters such as displacement thickness (δ^*), momentum thickness (θ), shape factor (H) and skin friction coefficient (C_f) are used to characterize the state of the boundary layer. The displacement thickness (δ^*) is defined as the wall-normal distance by which the boundary layer would be displaced to compensate for the reduction in mass flux due to viscous effects. It is given mathematically by:

$$\delta^* = \int_0^\infty \left(1 - \frac{U}{U_e}\right) dy \tag{2.1}$$

where U is the local streamwise mean velocity and U_e is the freestream mean velocity.

The momentum thickness (θ) is defined as the wall-normal distance by which the boundary layer would be displaced to compensate for the reduction in momentum flux due to viscous effects. Mathematically, θ is defined as:

$$\theta = \int_0^\infty \frac{U}{U_e}\left(1 - \frac{U}{U_e}\right) dy \tag{2.2}$$

The shape factor (H) is defined as the ratio of the displacement thickness to the momentum thickness, $H = \delta^*/\theta$. The skin friction coefficient (C_f) is a measure of drag the flow experiences and it is expressed mathematically as:

$$C_f = 2\left(\frac{U_\tau}{U_e}\right)^2 \tag{2.3}$$

where U_τ is the friction velocity.

A typical turbulent boundary layer can be divided into two distinct regions: (i) inner region and (ii) outer region. In the inner region, the flow dynamics is significantly altered by fluid viscosity, while the inertia effects are dominant in the outer region of the boundary layer. There is an overlap region between the inner and outer region when the Reynolds number is sufficiently high. In the inner region, the friction velocity, U_τ and the viscous length scale, $\delta_\nu = \nu/U_\tau$ (where ν is the kinematic viscosity) are the relevant velocity and length scales. The friction velocity and the viscous length scale are usually referred to as the inner variables and the superscript "$^+$" is used to denote quantities normalized by the inner variables. For instance, $U^+ = U/U_\tau$ and $y^+ = yU_\tau/\nu$, where U and y are respectively the mean velocity and wall-normal distance. According to Pope, 2000, the inner region extends from the wall ($y^+ = 0$) to $y^+ = 30$, the overlap region spans from $y^+ = 30$ to $0.2\delta^+$ while the outer region extends from $y^+ = 30$ to δ^+. The law of the wall ($U^+ = y^+$) is valid from $y^+ = 0$ to 5. In the overlap region, the distribution of the mean velocity is expressed by the classical logarithmic (log) law,

$$U^+ = \frac{1}{\kappa} ln y^+ + B \tag{2.4}$$

where κ is the von Kármán constant and B is the logarithmic constant.

The outer region of the boundary layer is usually examined by the maximum deviation of the measured data from the logarithmic law, ΔU_{max}^{+}, which is related to the strength of the wake parameter as $\Delta U_{max}^{+} = 2\Pi/\kappa$ (where Π is the wake parameter). Coles, 1956 demonstrated that the wake parameter increases with Reynolds number and asymptotes to a value of 0.55 at $Re_\theta \geq 6000$.

As stated earlier, there are two recirculation regions in a turbulent flow over FFS. The secondary recirculation bubble occurs in front of the step whereas the primary recirculation bubble occurs on top of the step. The primary recirculation region is characterized by significant flow reversals. For example, Essel et al., 2015 observed that the maximum streamwise backflow velocity is 15% of the approached freestream mean velocity. The shear layer that is separated by the leading edge of the step has streamwise fluctuations, known as flapping (Driver et al., 1987) which would cause the reattachment point on top of the step to oscillate within the reattachment region. Past studies have used different methods to determine the mean reattachment point. Westphal et al., 1984 suggested that the streamwise location where the flow moves forward 50% of the time can be used as a criterion to determine the mean reattachment point. Some of the other methods for determining the mean reattachment point include the mean dividing streamline, zero mean velocity, zero skin friction coefficient and zero stream function on the downstream wall. The distance from the leading edge of the step to the reattachment point is known as reattachment length (L_r) which is illustrated in Figure 2.1.

A new boundary layer develops after the reattachment point on top of the step. The recovering boundary layer is usually compared with a canonical turbulent boundary layer. The recovery or relaxation of the new boundary layer developed downstream of reattachment has been studied previously in wind tunnel (Bradshaw and Wong, 1972; Castro and Epik, 1998 and Jovic, 1996) and closed channel (Essel and Tachie, 2015; Shao and Agelinchaab, 2016). Bradshaw and Wong, 1972 suggested that the inner region of the new boundary layer recovers faster than the outer region while Castro and Epik, 1998 argued that the growth of the inner region is significantly affected by the outer region. Essel and Tachie, 2015 reported that the mean velocity and integral parameters recovered at 25 step heights from reattachment, however, Shao and Agelinchaab, 2016 could not observe similarity in the mean flow and turbulent quantities at 60 step heights downstream of the reattachment point.

2.2 Open channel turbulent flow

In many engineering and environmental applications such as irrigation systems, drainage systems and water and waste water treatment systems, a free-surface boundary condition is present. Therefore, it is important to understand the flow characteristics of open channel turbulent flow. In open channel flows, Froude number (Fr) is an important parameter for characterizing the flow features. The flow can be classified into the following three regimes using the Froude number based on the channel height and freestream velocity, $Fr = \frac{U_e}{\sqrt{(gH_u)}}$: subcritical regime ($Fr < 1$), critical regime ($Fr = 1$) and supercritical region ($Fr > 1$). These flow regimes affect the free-surface differently. For example, subcritical flows have the gentlest wavy surface whereas supercritical flows have a highly-disturbed surface with rapid waves.

The velocity and length scales for canonical turbulent boundary layers and fully developed closed channels are also used to analyze open channel turbulent flows. It has been observed in previous studies that the mean streamwise velocity and Reynolds stresses in the inner region of open channel flows compare well with those obtained in other canonical near-wall turbulent flows (Tachie et al., 2003; Afzal et al., 2009). However, in the outer region, because of the presence of the free surface, open channel flows have considerably higher freestream turbulence level which may significantly change some aspects of the boundary layer. For instance, compared to the canonical zero pressure gradient turbulent boundary layers at similar Reynolds numbers, the skin friction coefficient increases and wake region decreases due to the higher level of turbulence of open channel flow (Tachie et al., 2003; Afzal et al., 2009).

2.3 Rough wall turbulent boundary layer

As mentioned earlier, wall roughness is a defining feature in many engineering and environmental applications. Nikuradse's equivalent sand grain roughness (k_s) in inner variables (which is often referred to as equivalent sand grain Reynolds number $k_s^+ = \frac{U_\tau k_s}{\nu}$) is used exclusively to characterize the state of wall roughness. Based on the equivalent sand grain Reynolds number, Schlichting and Kestin, 1979 proposed that a surface can be classified into three different rough regimes: hydrodynamically smooth for $k_s^+ < 5$, transitionally rough for $5 \leq k_s^+ \leq 70$ and fully rough for $k_s^+ > 70$. Previous studies (Shao and Agelinchaab, 2016; Ren and Wu, 2011) have demonstrated that the mean streamwise velocity profile for rough wall in the outer layer is less uniform compared to the smooth wall at a comparable Reynolds number. As a result, the shape

factor and the skin friction coefficient are increased significantly with increasing k_s^+. Wall roughness may also increase the magnitude of the higher order turbulent statistics.

2.4 Previous studies on separated and reattached flows

Numerous studies have been performed over the last past decades to investigate the flow characteristics of separated and reattached turbulent flows over a FFS. It is recognized from these studies that the flow characteristics over FFS are dependent on a combination of fluid and flow parameters such as initial boundary layer condition, relative boundary layer thickness ($\frac{\delta}{h}$), Reynolds number based on step height and freestream mean velocity (Re_h), freestream turbulence level (T_u), aspect ratio, $AR = \frac{W}{h}$ (where W is the spanwise width of the channel) and blockage ratio, $BR = \frac{h}{H_u}$ (where H_u is the upstream channel height).

A summary of previous studies that investigated the flow characteristics of FFS is presented in Table 2.1. The table includes measurement techniques, blockage ratio (BR), Reynolds number (Re_h), reattachment length (L_r) and the flow quantities used to investigate the flow characteristics. It should be noted that LDV denotes laser Doppler velocimetry, HWA refers to hotwire anemometry and DNS denotes direct numerical simulation. The streamwise and wall-normal mean velocities are U and V respectively, $u'$and v' are the fluctuating components respectively in the streamwise and wall-normal directions, $\overline{u'^2}$ and $\overline{v'^2}$ are the streamwise and wall-normal Reynolds normal stresses

Table 2.1: Summary of previous studies on separated and reattached flows.

Author(s)	Geometry	Wall condition	Technique	Re_h	L_r/h	Quantities reported
Largeau and Moriniere, 2007	Forward facing step	Smooth	PIV	28800-128200	3.5-3.75	U, V, $\overline{u'^2}$, $\overline{v'^2}$, C_p, $-\overline{u'v'}$
Sherry et al., 2010	Forward facing step	Smooth	PIV	1400-19000	1.9-4	δ/h, $\overline{u'^2}$, $-\overline{u'v'}$
Hattori and Nagano, 2010	Forward facing step	Smooth	DNS	900-3000	2.04, 1.82, 2.01	U, $-\overline{u'v'}$, k, C_f
Awasthi et al., 2012	Forward facing step	Smooth	HWA	6640-213000	1.6-4.2	$\overline{u'^2}$, $-\overline{u'v'}$, C_p, P_{rms}
Tachie et al., 2001	Forward facing step	Smooth	LDA	960-1890	-	U, x_R, C_f, H, G
Ren and Wu, 2011 and 2013	Forward facing step	Smooth, rough	PIV	3450	1.17	U, $\overline{u'^2}$, $\overline{v'^2}$, $-\overline{u'v'}$, ω, *pdf*,
Essel et al., 2015 Essel and Tachie, 2015	Forward facing step	Smooth, rough	PIV	2230-8950	1.20-1.40	U, V, $\overline{u'^2}$, $\overline{v'^2}$, $-\overline{u'v'}$, H, C_f, G, Π, R_{uu}, R_{vv}, L^u_y, L^v_y
Shao and Agelinchaab, 2016	Forward facing step	Smooth, rough	PIV	1600-4800	1.3-2.3	U, V, $\overline{u'^2}$, $\overline{v'^2}$, $-\overline{u'v'}$, P_{uu}, P_{vv}, P_{uv}, *Budget terms*

respectively, $-\overline{u'v'}$ refers to the Reynolds shear stress, P_{uu}, P_{vv} and P_{uv} are the production of Reynolds normal and shear stresses, ν_t is the kinematic eddy viscosity, C_p is the pressure coefficient, P_{rms} is the root mean square of wall pressure, $\overline{u'^3}$, $\overline{u'^2v'}$, $\overline{u'v'^2}$ and $\overline{v'^3}$ are the triple velocity correlations. The vorticity and the vorticity thickness are denoted by ω and δ_ω respectively, P_k is the production of turbulent kinetic energy, *pdf* is the probability density function, R_{uu} and R_{vv} are the streamwise and wall-normal two-

point auto correlation functions respectively and L^u_y and L^v_y are the wall-normal integral length scales of streamwise and wall-normal velocity fluctuations respectively.

Largeau and Moriniere, 2007 investigated the effects of $\frac{W}{h}$ and $\frac{\delta}{h}$ on reattachment length for a wide range of Reynolds numbers ($28800 \leq Re_h \leq 128200$) and observed that the reattachment length increased as much as 7% when $\frac{W}{h}$, $\frac{h}{H_u}$ and $\frac{\delta}{h}$ were decreased. On the other hand, with an increase of blockage ratio, the acceleration of the flow over the step increases which leads to a larger velocity gradient, enhanced mixing and entrainment, and a shorter reattachment length.

The effects of Reynolds number on flow separation and reattachment have been studied in great detail. Sherry et al., 2010 investigated the effects of Re_h and $\frac{\delta}{h}$ on FFS immersed in a turbulent boundary layer. The Reynolds number Re_h was varied from 1400 to 19000 and for $0.83 \leq \frac{\delta}{h} \leq 2.5$. It was observed that, for a given $\frac{\delta}{h}$, L_r increased linearly with Re_h up to 8500, beyond which no significant increase was observed in L_r. It was reported that when $\frac{\delta}{h} < 1$, the influence of upstream boundary layer is minimal. Conversely when $\frac{\delta}{h} > 1$, the reattachment length is significantly affected by the Re_h.

The state of the upstream boundary layer over a FFS was studied by Hattori and Nagano, 2010 using DNS for Re_h = 900 to 3000 and $\frac{\delta}{h} \approx 1.5$ to 3. A counter gradient diffusion (CDP) phenomenon was observed at the low Reynolds number (Re_h = 900) but this phenomenon vanished at higher Reynolds numbers (Re_h = 1800 and 3000). The profiles of mean velocity and Reynolds stresses were also examined. Quadrant analysis was performed to investigate the turbulence motions around the step. It was observed that the

ejection events contributed more to the production of Reynolds shear stress than sweeps even though ejections occurred further away from the wall and sweeps dominated in the near wall region.

Awasthi et al., 2012 performed an experimental study using hot wire anemometry. The Reynolds number, Re_h ranged from 6640 to 213000 and relative boundary layer thicknesses $\frac{\delta}{h}$ were 0.038, 0.15 and 0.6. Similar to the study of Sherry et al., 2010, two regimes were found: the first regime is for $Re_h < 3000$ where L_r is a strong function of Reynolds number and the second regime is for $Re_h > 3000$ where L_r is independent of Reynolds number.

Essel et al., 2015 investigated the effects of Reynolds number on separated and reattached turbulent flow over FFS. The experiments were performed using PIV at different Reynolds numbers ($2040 \leq Re_h \leq 9130$). Two different regimes of L_r were observed similar to the study of Sherry et al., 2010; however, the transition Reynolds number ($Re_h = 6380$) was lower than reported by Sherry et al., 2010. At similar Re_h and $\frac{\delta}{h}$, the reattachment length was 40% shorter than reported by Sherry et al., 2010 which is likely due to higher turbulence intensity and blockage ratio.

In a subsequent study, Essel and Tachie, 2015 investigated the effects of Reynolds number on the turbulence structures in the recovery regions of a FFS. The mean velocities and integral parameters recovered at 25 step heights from reattachment but Reynolds stresses would require longer streamwise distances to fully recover. The results showed that $\overline{u'^2}$ recovered faster than $\overline{v'^2}$ and $\overline{-u'v'}$. For example, at 25 step heights downstream of reattachment point and $y/\delta = 0.5$, $\overline{u'^2}$ was within 5% of the upstream

value whereas $\overline{v'^2}$ and $\overline{-u'v'}$ were within 11% and 9% respectively of their respective upstream values. In order to examine the effects of Reynolds number on the spatial coherence of the turbulence structures, two point correlation functions and integral length scales were used. The integral length scales were found to be independent of Reynolds number. Quadrant analysis revealed that ejections and sweeps are the major contributors to positive Reynolds shear stress on the step and outward and inward interaction motions are the major contributors to negative Reynolds shear stress near the leading edge.

Tachie et al., 2001 investigated the recovery of boundary layer downstream of a separated turbulent flow over FFS in an open channel at Re_h ranging from 960 to 1890. It was observed that the mean velocity profiles collapsed onto the corresponding upstream profiles at $x/h \geq 50$. However, even at x/h = 100, the streamwise turbulence intensity profiles did not collapse on the upstream profiles.

In comparison to the large number of studies conducted for separated and reattached turbulent flows over smooth FFS, there are only a handful of studies (Ren and Wu, 2013; Essel et al., 2015; Essel and Tachie, 2015; Shao and Agelinchaab, 2016) that investigated roughness effects on separated and reattached turbulent shear flows over a FFS. Therefore, our understanding of the effects of roughness on the flow characteristics over a FFS is limited to information provided in these studies.

Ren and Wu, 2013 investigated the effects of the roughness on separated and reattached flow over FFS in a wind tunnel. A PIV technique was used to perform velocity measurements over both smooth and rough steps at the same Reynolds number, Re_h = 3450 and δ/h = 8. A three dimensional and highly irregular topographical roughness

element from a realistic turbine blade was used as the roughness element. The roughness elements were placed on top wall of the FFS while the upstream wall was kept smooth. The results showed that wall roughness reduced the mean velocities as well as the turbulence statistics. Quadrant analysis revealed that roughness reduced the shear stress contributions from both ejections and sweeps.

Essel et al., 2015 and Essel and Tachie, 2015 investigated the effect of upstream roughness on the reattachment and recovery regions downstream of a FFS in a closed channel. Sand grain of mean diameter 1.5 mm was used as the upstream roughness element. At lower Reynolds numbers ($Re_h \leq 5100$), the roughness condition was in the transitional regime ($k_s^+ < 70$), but it became fully rough ($k_s^+ > 70$) at higher Reynolds numbers ($Re_h \geq 6480$). At comparable Re_h, the upstream rough wall reduced the reattachment length by 40% compared to the smooth wall value. It was argued that the reduction in L_r was not due to the upstream roughness solely but due to the reduction in mean velocity and the higher turbulence level in the shear layer. The turbulent kinetic energy and Reynold shear stress were independent of the upstream condition in the immediate vicinity of the wall because the separated shear layer created a protective shield for the separation bubble and the local APG mitigated the roughness effect. In the separation bubble, the integral scales were independent of the upstream roughness but further away, roughness increased the size of these scales. In the recovery region, the effect of upstream roughness gradually decreased as the boundary layer developed further downstream.

Most recently, Shao and Agelinchaab, 2016 used a rough FFS and a smooth upstream wall in a closed channel to investigate the effect of surface conditions on separation

bubble and mean statistics. Three Reynolds numbers, Re_h = 1600, 3200 and 4800 were investigated. Sandpaper 24 grits and sandpaper 36 grits were used as the roughness elements and the equivalent sand grain roughness were 1.37 mm and 1.70 mm respectively. The results indicated that the reattachment length increases with Reynolds number from 1.7 to 2.3 for the smooth wall. Wall roughness was observed to decrease the reattachment lengths. For example, the reattachment lengths for sandpaper 24 grits and 36 grits were 48% and 26% shorter than the reattachment length of the smooth wall at Re_h = 4800. The mean velocity profiles and turbulent quantities over the smooth and rough step did not achieve similarity at 60 step heights downstream of the leading edge of the step.

Apart from the aforementioned studies, there are a few other investigations which are relevant to the present study. Ampadu-Mintah and Tachie, 2015 investigated wall roughness effects on turbulent flow over a BFS in an open channel. Sand grain was used as the roughness element. The study was conducted at Re_h = 3240 and measurements were obtained up to 60 step heights downstream of the trailing edge of the step. It was observed that wall roughness had no significant effects on the mean and turbulent quantities in the recirculation and early recovery region, and attained self-similarity at 32 step heights from the trailing edge of the step.

Kim and Chung, 1995 investigated wall-roughness effects on turbulent flow downstream of a smooth BFS. In this study, two-dimensional traverse square ribs of varying pitch-to-height ratio, p/k = 1.43, 3.50 and 5.71 were used in the bottom wall downstream of the step. A split film sensor was used to measure the velocity field. For the smooth downstream wall and p/k = 1.43 ribs, the reattachment length was 5.68h; however,

increasing the p/k to 5.71 increased the reattachment length by 3.4%. In the recovery region, the streamwise mean velocity profiles recovered faster over the rib-roughen walls compared to that of the smooth wall.

2.5 Summary of previous studies

The review of previous works on separated and reattached turbulent shear flows showed that the flow behavior over a FFS is affected by a combination of fluid and flow parameters such as initial boundary layer state, Reynolds number, blockage ratio, aspect ratio, freestream turbulence and wall roughness. A higher level of freestream turbulence and blockage ratio decrease the reattachment length considerably. The recovery of the flow after the reattachment is a slow process and takes several step heights to recover due to a slow breakdown of the large scale to small scale structures. To date, only Tachie et al., 2001 examined the characteristics of separated and reattached turbulent flows over FFS in an open channel. Moreover, there is no study that investigated roughness effects on flow over FFS in an open channel. Therefore, the effects of roughness on flow separation and subsequent reattachment and recovery downstream of a FFS in an open channel are not yet well understood.

CHAPTER 3

EXPERIMENTAL SETUP AND MEASUREMENT PROCEDURE

This chapter presents a description of the test facility, test sections and test conditions. The measurement procedure employed to conduct the velocity measurements using PIV technique is also discussed.

3.1 Experimental setup

3.1.1 Test facility

The experiments were performed in a recirculating open water channel which was designed and manufactured by Engineering Laboratory Design, Inc., Minnesota, USA. The components of the water channel include flow settling chamber, centrifugal pump, variable speed drive, piping system, supporting framework and a filtering system. The main recirculating channel has dimensions of 2500 mm (length) × 200 mm (height) × 200 mm (width) and shown in Figure 3.1. The side and bottom walls are fabricated with Super Abrasive Resistant® (SAR) clear acrylic plate to facilitate optical access and flow visualization. The motor that drives the centrifugal pump has a 24 HP transistor inverter type variable speed controller. A filtering system is used to remove contaminants from the circulating water.

3.1.2 Test section

Figure 3.2 (a) shows the schematic diagram of the side view of the test section (with relevant dimensions) which was fabricated and inserted into the main open water tunnel. The walls of the test section are made of 6 ± 0.1 mm transparent acrylic plate to facilitate

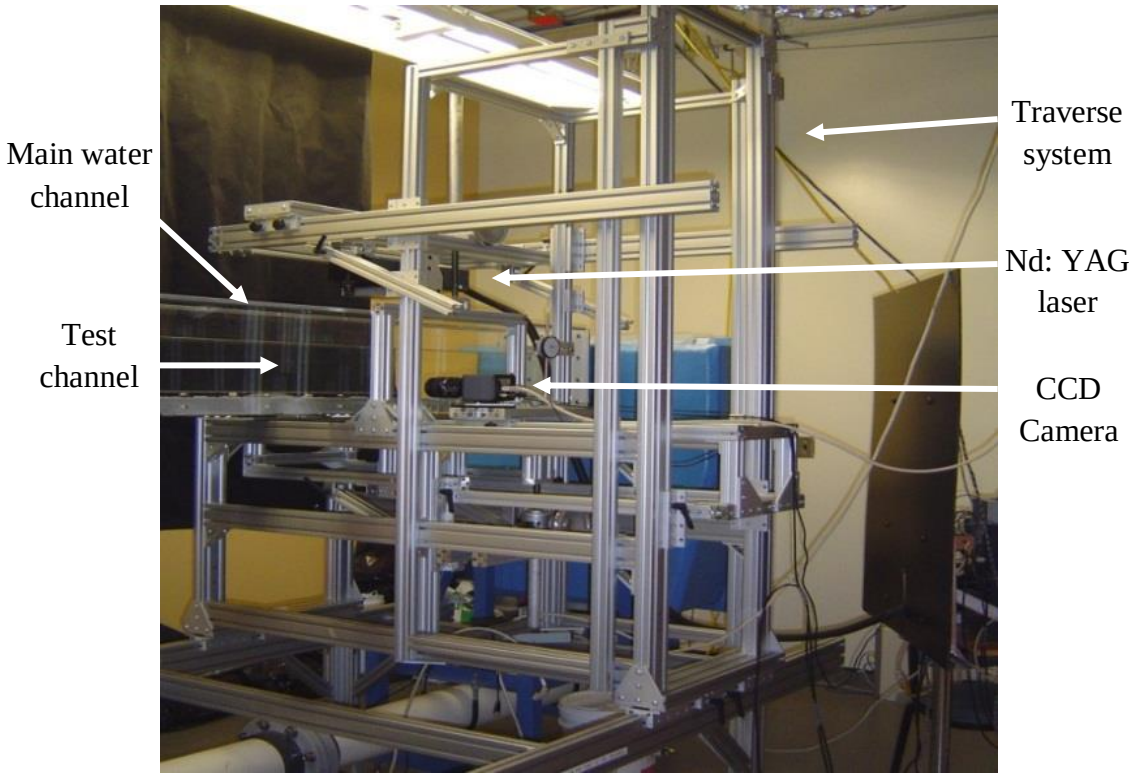

Figure 3.1: Picture of the main recirculating water tunnel and relevant components.

optical access. The thickness of the side walls reduced the internal width of the test section. Thus, the final dimensions of the test section are 2500 mm (length) × 60 mm (height) × 186 mm (width). The flow was tripped with a 3.5 mm square rib to accelerate the development of the turbulent boundary layer. The trip was placed on the bottom wall at the inlet section and spanned the width of the channel. A FFS of nominal height, h = 12 mm was positioned at 1255 mm from the entrance of the test channel. The upstream water depth H_u was kept constant at 60 mm. The present aspect ratio, $\frac{W}{h}$ = 15.5 is larger than the threshold value of 10 required to ensure the mean flow is nominally two dimensional at the mid span of the channel (Largeau and Moriniere, 2007; Brederode and Bradshaw, 1972).

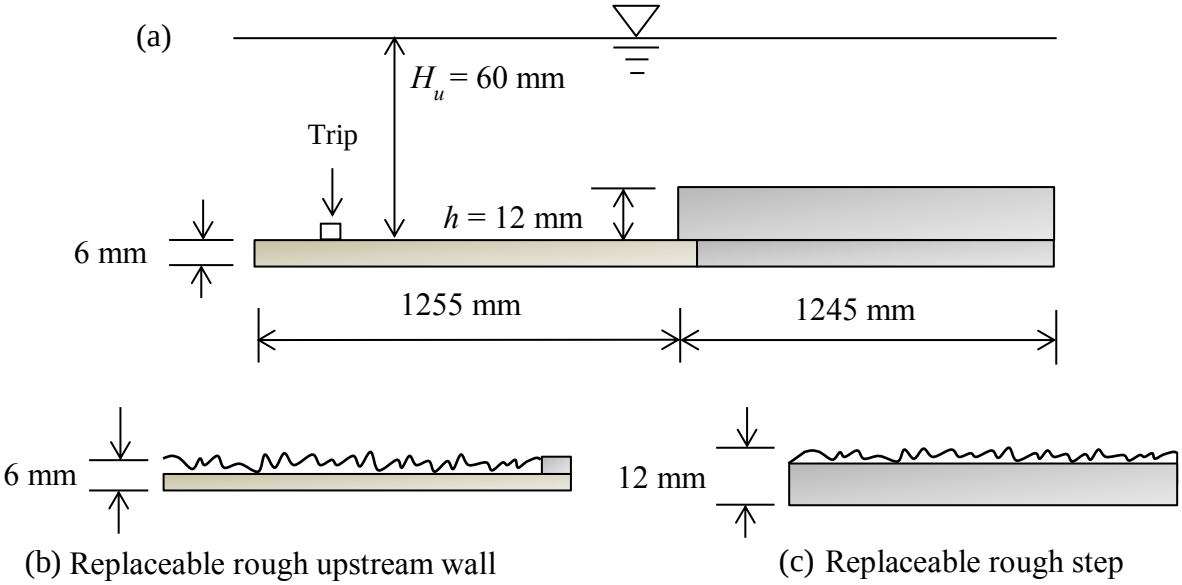

Figure 3.2 (a) Schematic diagram of the test channel with the replaceable (b) upstream rough wall and (c) rough FFS (*not drawn to scale*).

The length of the FFS to step height, $\frac{L}{h}$ = 103 was significantly large to ensure reattachment on top of the step (Bergeles and Athanassiadis, 1983). The blockage ratio $\frac{h}{H_u}$ in this study was 0.2 which is the same ratio in the study by Essel et al., 2015 and Essel and Tachie, 2015. This similarity is necessary to facilitate comparison of the present results to those reported by Essel et al., 2015.

3.2 Surface conditions

Three upstream wall conditions were investigated; (i) smooth wall produced from 6 mm acrylic plate and rough walls produced from (ii) sandpaper 36 grit and (iii) sand grains (Figure 3.2(b)). The sandpaper had a mean thickness of 1.5 mm and was glued onto a 4.5 mm acrylic plate to produce a roughness plate of equivalent height of 6.0 ± 0.1 mm. Similarly, the sand grains of mean diameter 1.5 mm were glued onto a 4.5 mm acrylic

plate and the resulting height of the plate was 6.0 ± 0.1 mm. Two downstream wall conditions were investigated; (i) a smooth replaceable step produced from a 12 mm acrylic plate and glued onto 6 mm acrylic plate, and (ii) a replaceable rough step made from sandpaper 36 grit glued onto a 10.5 mm acrylic plate which gives a combined thickness of 12 ± 0.1 mm (Figure 3.2(c)). For brevity, the upstream and downstream smooth experiment is denoted by SM-SM, upstream sandpaper and downstream smooth experiment is denoted by SP-SM, upstream sand grain and downstream smooth experiment is denoted by SG-SM and upstream and downstream sandpaper experiment is denoted by SP-SP.

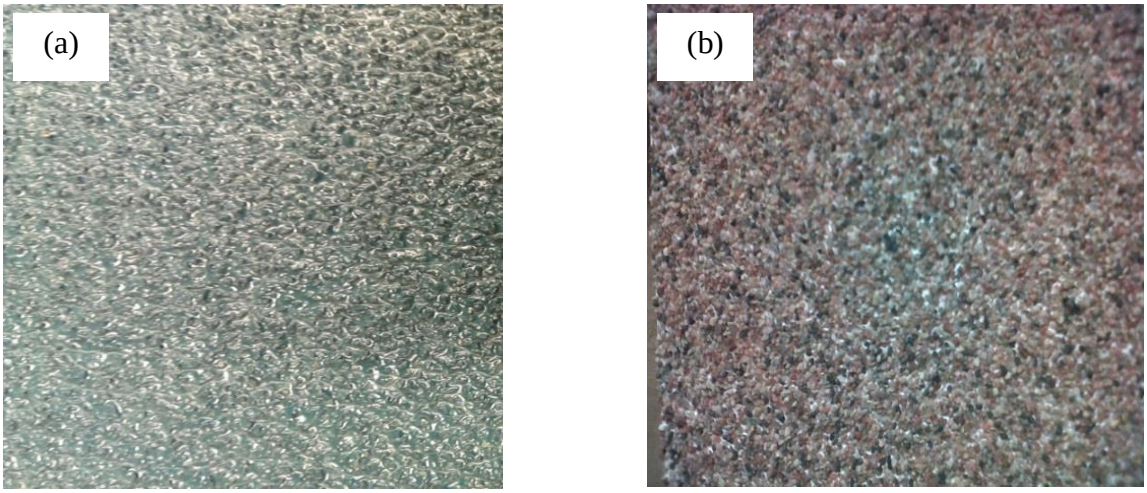

Figure 3.3: (a) Sandpaper 26 grit and (b) sand grain used to investigate roughness effects.

A Veeco Wyco NT9100 optical profilometer was used to obtain the topographical information of the roughness elements. The profilometer uses white light interferometry with sub-micron vertical accuracy. Figure 3.3 shows pictures of the sandpaper 36 grit and sandpaper and the roughness statistics are summarized in Table 3.1. The average peak-to-trough roughness heights is denoted as k_t, the root-mean-square roughness height is

referred to as k_{rms}, while the skewness and flatness of the roughness probability density function are denoted as *Sk* and *Ku* respectively. The values of the equivalent sand grain roughness height, k_s were estimated using the formula proposed by Flack and Schultz, 2010:

$$k_s = 4.43 k_{rms}(1 + Sk)^{1.37} \tag{3.1}$$

Table 3.1 Surface statistics of rough surface

Surface condition	k_t (mm)	k_s (mm)	k_{rms} (mm)	*Sk*	*Ku*
Sandpaper 36 grit	1.12	1.37	0.16	0.61	3.23
Sand grain	1.83	1.91	0.42	0.02	2.13

The equivalent sand grain roughness height, k_s for sandpaper 36 grit is approximately 20% larger than the corresponding average roughness height, k_t, while in the case of sand grain, k_s is approximately 4% higher. Table 3.1 shows that the value of k_s of sand grain is approximately 28% higher than that of sandpaper 36 grit, and the values of *Sk* imply that there are more peaks than troughs on sandpaper 36 grit compared to the sand grain roughness.

3.3 PIV system

The velocity measurements were performed using the particle image velocimetry (PIV) technique. The PIV is a non-intrusive multi-point velocity measurement technique which is directional sensitive. Therefore, the PIV can measure instantaneous positive and negative velocity vectors simultaneously at thousands of locations within the whole flow field. The following sections provide information about the working principle of PIV,

characteristics of the seeding particles, the light source and the recording medium used in the present PIV system.

3.3.1 Working principle of PIV

In PIV technique, the flow is seeded with tracer or seeding particles and the flow field is illuminated by two pulses of laser sheet separated by a time delay, Δt. The scattered lights reflected by the seeding particles are captured using a couple-charged device (CCD) camera on two successive images which are called image pairs. In order to obtain the velocity vectors, each image pair is divided into grids of interrogation area (IA). A numerical correlation algorithm is applied for each IA to statistically determine the local displacement vector, Δs of the particles between the image pairs, i.e. between the first and the second image. The velocity vector within the IA is then obtained by dividing the average of local displacement vector, Δs by the time delay Δt. The velocity vector map of the whole flow field is obtained by repeating the numerical correlation algorithm for all the IAs.

3.3.2 Characteristics of the seeding particles

The various components of the PIV system are shown in Figure 3.1. The PIV system comprised of double pulsed laser, CCD camera and synchronizer (not shown in figure). The flow was seeded with fluorescent polymer particles (Rhodamine B) of mean diameter 10 μm. The specific gravity and the refractive index of these particles are 1.19 and 1.48 respectively. The PIV technique measures the velocity of the tracer particles and not the velocity of fluid. In order to ensure that the particles faithfully follow the fluid, the particles settling velocity and response time were determined. The settling velocity, v_s was evaluated using the following equation given by Mei et al., 1991:

$$v_s = \frac{(\rho_p - \rho_f) g d_p^2}{18 \mu_f} \tag{3.2}$$

Here, ρ_p is the particle density, ρ_f is the fluid density, g is the gravitational acceleration, d_p is the diameter of the particle and μ_f is the dynamic viscosity of the fluid.

The response time, t_r, characterizes the ability of the particle to follow the fluid and it is a measure of the tendency of the particles to attain velocity equilibrium with the fluid. The response time, t_r, for the particle was obtained using the formula given by Raffel et al., 1998:

$$t_r = \rho_p \frac{d_p^2}{18 \mu_f} \tag{3.3}$$

The values of the settling velocity and response time of the particles were $v_s = 1.04 \times 10^{-6}$ m/s and $t_r = 6.61 \times 10^{-6}$ s, respectively. The settling velocity and the response time are negligibly small compared to the streamwise mean velocity and sampling time respectively used in the present study as will be shown subsequently. It was therefore concluded, based on the particles response time and settling velocity that the seeding particles follow the flow faithfully.

3.3.3 Light source

A New Wave Solo Nd:YAG double pulsed laser was used to illuminate the flow field. This laser emits green light of 120 mJ/pulse at 532 nm wavelength and a maximum repetition rate of 15 Hz. A 12-bit CCD camera with 2048 × 2048 pixel array and 7.4 μm pixel pitch was used to capture the scattered lights reflected by the particles. The trigger rate of the laser and image capturing time of the CCD camera were controlled by a synchronizer. The fluorescent seeding particles absorb the green laser light and emit

orange light at 570 nm wavelength. The CCD camera was equipped with an orange filter with band-pass wavelength of 570 nm. This orange filter together with the fluorescent polymer particles helped to reduce reflection and surface glare from the interface between the working fluid and the wall, thereby significantly improved the quality of the velocity vectors close to the wall.

3.3.4 Data acquisition and measurement procedure

A commercial software, DynamicStudio verson 4.10 (supplied by Dantec Dynamics Inc.), was used for the data acquisition. For each wall condition, detailed velocity measurements were performed at 9 different *x*-*y* planes which are illustrated in Figure 3.4. The sampling frequency was set to 4 Hz. The field of view for each of these planes was set to 70 mm × 70 mm which is 5.8*h* × 5.8*h* (where *h* is the step height). To characterize the upstream boundary layer, a plane PA which spanned from x/h = -25 to -19.2 was used. Two planes, P0 and P1 were used to investigate the turbulent characteristics in the separated shear layer between the ranges of $-4.7 \leq x/h \leq 4.3$. To examine the redevelopment region, measurements were acquired in six different planes (P2 - P7) which spanned $5 \leq x/h \leq 60$. Based on preliminary convergence test, a sample size of 5000 instantaneous image pairs was acquired in each plane. The acquired images were post processed using adaptive correlation and moving average validation options of DynamicStudio v4.10. In the adaptive correlation algorithm, a multi-pass fast Fourier transform cross-correlation algorithm with a one-dimensional Gaussian peak-fitting function is used to determine the average particle displacement within an interrogation area to subpixel accuracy.

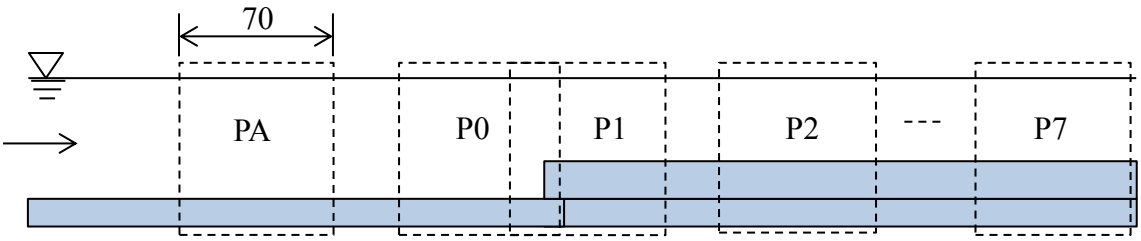

Figure 3.4: Different measurement planes

3.3.5 Spatial resolution

An interrogation area (IA) size of 32 pixel × 32 pixel with 50% overlap was employed to process the instantaneous velocity data. The spacing between adjacent vectors was Δx × Δy = 0.55 mm × 0.55 mm resulting in a spatial resolution of 0.046h × 0.046h. The wall-normal spacing between adjacent vectors Δy, was also compared with the Kolmogorov length scale (η) and Taylor microscale (λ). In the upstream plane, η and λ were estimated using the procedure outlined in previous turbulent boundary layer studies (Johansson and Alfredsson, 1983) and in the recirculation region η was calculated following the procedure described in Piirto et al., 2003. The values of Kolmogorov length scale and Taylor micro-scale were calculated directly from the experimental data, using $\eta = (\nu^3/\varepsilon)^{0.25}$ and $\lambda = \sqrt{\overline{u^2}/\overline{(\partial u/\partial x)^2}}$, where ε, the mean dissipation rate, was estimated as $\varepsilon = 15\nu\overline{(\partial u/\partial x)^2}$. It was found that $\Delta y/\eta$ = 3.2 and $\Delta y/\lambda$ = 0.3, which demonstrate that the IA is larger than the smallest scales (Kolmogorov). The Kolmogorov scales are responsible for the dissipation of turbulent kinetic energy; therefore, the present resolution is not adequate to accurately measure the dissipation rate. On the other hand, the IA is smaller than the Taylor micro-scale, therefore, the resolution is to adequately resolve the turbulence statistics (e.g. Reynolds stresses, triple velocity correlations) reported in this study.

3.3.6 Measurement uncertainty

Bias and precision errors are two sources of errors upon which the estimation of accuracy of the PIV system depends. Precautionary guidelines and advanced evaluation algorithms were used during the data acquisition and post-processing to minimize both the bias and precision errors (Prasad et al., 1992 and Forliti et al., 2000). Sources of bias errors include inaccuracy in magnification factor and time between pulses (Δt), response time of the seeding particles and optical distortion of the lens system. Maximum particle displacement was limited to 1/4 of the interrogation area size to minimize bias errors due to loss of image pairs and peak-locking effect. On the other hand, the precision errors are associated with the computation of averaged mean and turbulence statistics from the instantaneous image pairs. Following the procedure recommended by Casarsa and Giannattasio, 2008, a large sample size (5000) was used to calculate the mean velocity and higher order moments. The use of such a large sample size helped to average out the precision and sampling error. For 95% confidence level, the equation for mean and fluctuating velocities and Reynolds shear stress are as follows:

$$\varepsilon_U = \frac{s\,[U]}{|U|} = \frac{Z_c}{\sqrt{N}}\frac{\sqrt{u'^2}}{|U|}; \quad \varepsilon_{\sqrt{u'^2}} = \frac{s[\sqrt{u'^2}]}{\sqrt{u'^2}} = \frac{Z_c}{\sqrt{2N}}; \quad \varepsilon_{\overline{u'v'}} = \frac{s|\overline{u'v'}|}{|\overline{u'v'}|} = \frac{Z_c}{\sqrt{N}} \qquad (3.4)$$

where s is the estimated standard deviation, Z_c is the confidence coefficient which is equal to 1.96 for 95% confidence level, N is the sample size, U is the streamwise mean velocity, $\sqrt{u'^2}$ is the root-mean square of the streamwise fluctuating velocity and $\overline{u'v'}$ is the Reynolds shear stress. The uncertainty of the mean streamwise velocity was estimated to be 1.4% except within the recirculation bubble where the uncertainty was as high as 10% because of the relatively low mean velocity and high fluctuating velocities within

the recirculation bubble. The uncertainties in the turbulence intensities and Reynold shear stress are 2% and 2.8% of the peak values, respectively.

CHAPTER 4

RESULTS AND DISCUSSION

In this chapter, the characteristics of the mean flow and turbulence statistics will be presented and discussed. The chapter is organized into three main sections. The first section discusses the characteristics of the approach flow in the upstream region prior to separation. The second section provides discussion on the effects of wall roughness on the flow characteristics in the separated and reattached regions, while the third section focuses on the investigation of the effects of wall roughness on the flow characteristics in the recovery region.

4.1 Upstream boundary layer characteristics

The characteristics of upstream boundary layer have a significant effect on the separation and reattachment process. A summary of the salient properties of the approach boundary layer over the smooth and rough walls is presented in Table 4.1. Recall that these measurements were taken at x/h = -22.1 which is well upstream of the step; therefore, the step has no effects on these results. The relative boundary layer thickness ($\frac{\delta}{h}$), displacement thickness ($\frac{\delta^*}{h}$) and momentum thickness ($\frac{\theta}{h}$) are also included in Table 1. The results indicated that upstream wall roughness increased the mass deficit ($\frac{\delta^*}{h}$) and momentum deficit ($\frac{\theta}{h}$) compared to the smooth wall. For instance, compared to the smooth wall, the mass deficit was increased by 3.7% and 14.6% respectively, over the sandpaper and sand grain. The Reynolds number based on momentum thickness, Re_θ ranged from 1920 to 2180 over the smooth and rough walls. The Re_θ obtained over the

smooth wall is comparable to 1940 reported over the smooth wall in the study of Essel et al., 2015 but lower than 3130 reported in the study of Ren and Wu, 2011. The effect of wall roughness on the upstream boundary layer is further investigated using the shape factor, $H = \frac{\delta^*}{\theta}$. The shape factor for the smooth wall was 1.33 but upstream wall roughness increased the shape factor, especially for the case of sand grain which showed 8% increase compared to smooth wall value.

Table 4.1: Properties of approach boundary layer over smooth and rough upstream walls.

	SM	**SP**	**SG**
U_e **(m/s)**	0.267	0.272	0.283
Re_H	16030	16350	17010
Re_h	3210	3270	3400
Re_Θ	1920	1980	2180
T_u **(%)**	4.28	4.65	4.76
δ/h	4.78	4.78	4.57
δ^*/h	0.82	0.85	0.94
θ/h	0.60	0.61	0.64
H	1.33	1.35	1.44
C_f	0.0039	0.0041	0.0065
Π	0.28	0.31	0.36
k_s^+	-	5	48

The streamwise mean velocity profiles over the smooth and rough walls in the outer coordinates are shown in Figure 4.1 (a). The characteristic velocity and length scales used here are U_e and H_u, respectively. The upstream water height, H_u is used as the characteristic length scale in preference over the traditional boundary layer thickness to examine the flow behaviour up to the free-surface. The position of the step relative to the upstream water height is shown by the dotted line. The figure shows that the mean velocities vary from the no-slip boundary condition at the wall (y = 0) to its freestream value. The effect of roughness is clearly evident; for example, the velocity profiles over

the rough walls are less "full" compared to the smooth wall, which is attributed to the higher drag experienced over the rough walls. At y/H_u = 0.2, for example, the mean velocity over the smooth wall and sandpaper are about $0.76U_e$ and $0.74U_e$ respectively. Meanwhile, the mean velocity over the sand grain wall was reduced by 10% compared to the smooth wall.

The mean velocities in the inner coordinates are shown in Figure 4.1 (b). In this figure, the mean velocity was fitted onto the classical logarithmic law $U^+ = \frac{1}{k} lny^+ + B$. The log law constants adopted in the present study are κ = 0.41 and B = 5.0. The mean velocity profile over the smooth wall follows the logarithmic law in the range $30 \leq y^+ \leq 500$. The traditional downward-right roughness shift (ΔB^+) can be observed for the rough-wall profiles, and the shape of the profiles are strongly dependent on the specific roughness elements. The profile over sandpaper shifted only a little from the corresponding smooth-wall profile.

The equivalent sand grain roughness Reynolds number, k_s^+ was calculated using the equation: $\Delta B^+ = \left(\frac{1}{\kappa}\right)\ln(k_s^+) + B - 8.5$ and the values are shown in Table 4.1. It can be observed from Table 4.1 that the roughness conditions for the sandpaper and sand grain are in transitional rough regime ($k_s^+ < 70$), even though the k_s^+ value for the sand grain is significantly larger than for sandpaper. The roughness condition for sandpaper ($k_s^+ = 5$) is in early transitional regime which explains the close similarity between the mean velocity profiles over the smooth and sandpaper in both inner and outer coordinates.

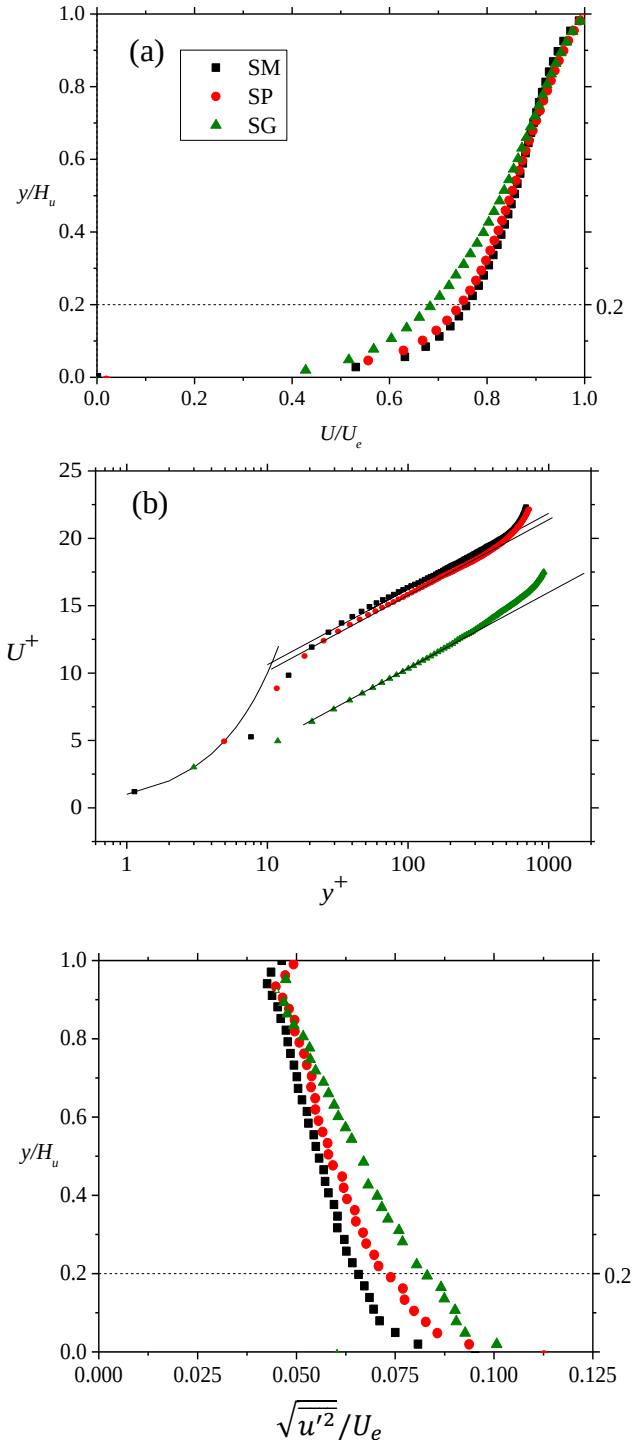

Figure 4.1 Profiles of (a) streamwise mean velocity over smooth and rough walls in outer coordinates, (b) inner coordinates and (c) streamwise turbulence intensity in upstream region.

The friction velocity, U_τ estimated using the Clauser plot technique, was used to determine the skin friction coefficient and the values for the three test conditions are summarized in Table 4.1. The C_f value for the smooth wall is 0.0039. Wall Roughness increased the skin friction coefficient values in comparison to the smooth wall by 5% over the sandpaper and 67% over the sand grains.

The maximum deviation of the mean velocity (ΔU_{max}^{+}) in the outer region of the boundary layer was determined and used to evaluate the strength of the Coles wake parameter, Π (Fernholz and Finley, 1996). Upstream roughness increased the strength of the wake parameter, for example, the wake strength for the smooth wall was Π = 0.28, which increased to 0.31 and 0.36 respectively, for the sandpaper and sand grain roughness. The C_f value for the smooth wall compares well with 0.004 and 0.0042 reported in previous open channel turbulent flows (Afzal et al., 2009; Tachie et al., 2001). The value of Π for the smooth wall in the present study is higher than the values obtained in prior open channel turbulent flow studies (Afzal et al., 2009; Tachie et al., 2003) at similar Reynolds number but lower than Π obtained in zero pressure gradient (ZPG) turbulent boundary layer (Purtell et al., 1981). One should recall that for a typical smooth wall ZPG boundary layer, the strength of the wake parameter is 0.55 which is significantly different from the present values. This difference is attributed to the combined effect of free-surface and elevated turbulence levels in open channel flows (Tachie et al., 2003; Ampadu-Mintah and Tachie, 2015). The fact that the upstream roughness increased the strength of the wake parameter is also consistent with previous open channel and ZPG studies (Krogstad et al., 1992; Tachie et al., 2000).

The profiles of upstream streamwise turbulence intensities are shown in Figure 4.1 (c). The turbulence intensity at the edge of the boundary layer for the smooth wall is about 4.3% which is in good agreement with 4% obtained by Ampadu-Mintah and Tachie, 2015. The upstream rough walls increased the turbulence intensities mostly close to the wall. For example, at the same height of the step ($y = h$), the turbulence intensities over the sandpaper and sand grain increased by 12% and 21% respectively, compared to the smooth wall.

From the discussion above, it is evident that wall roughness considerably modified the upstream mean flow characteristics in comparison to the smooth wall. These modifications include increased mass and momentum deficit as well as the shape factor. It also increased the upstream turbulence levels close to the wall.

4.2 Recirculation bubble and reattachment region

4.2.1 Streamwise mean velocities and size of the recirculation bubble

Contour plots of the streamwise mean velocity for smooth and rough walls are shown in Figure 4.2 to reveal some qualitative aspects of the mean flow in the separation and reattachment regions. The freestream velocity U_e and the step height h were used as the velocity and length scales respectively in these plots. The physical size of the recirculation bubble is defined as the region enclosed by the $U/U_e = 0$ contour level and the top surface of the step. For each case, the approach boundary layer is deflected upwards immediately before the step and reattaches on the front face of the step. This separation and reattachment form a smaller or secondary recirculation bubble in front of

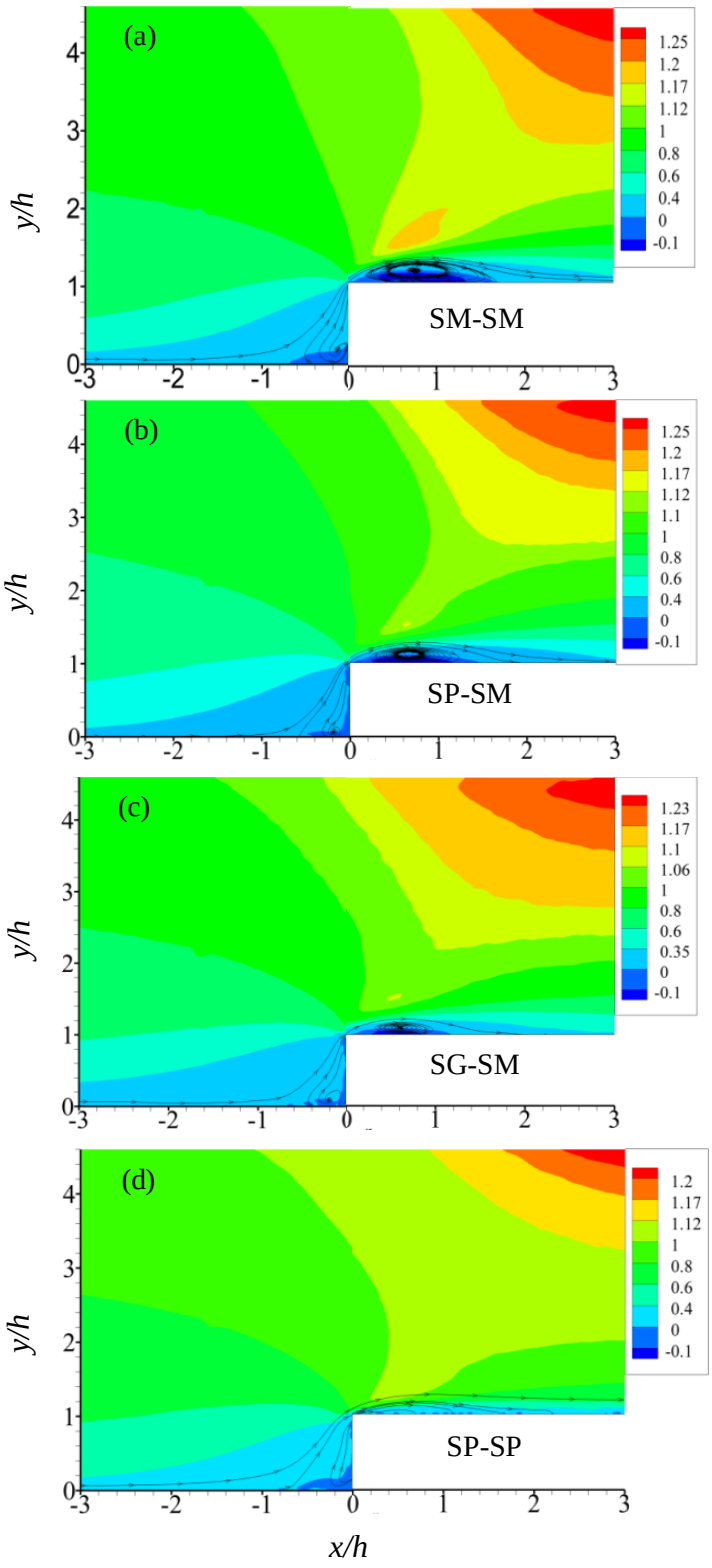

Figure 4.2 Contour plots of streamwise mean velocity for (a) SM-SM, (b) SP-SM, (c) SG-SM and (d) SP-SP in the recirculation region.

the step which can be observed in Figure 4.2. For the rough cases, the size of this upstream recirculation bubble is not clearly defined due to surface glare at the interface between the rough wall and fluid at the corner of the step which attenuated the quality of the data in that region. The flow separates again at the leading edge of the step and the separated shear layer reattaches on top of the step. As mentioned earlier, part of this shear layer is deflected upstream and forms a distinct larger or primary recirculation bubble while the other part redevelops into a new boundary layer downstream of the reattachment region. For the case of SP-SP, no distinct primary recirculation bubble was observed as can be seen from Figure 4.2 (d). The reason for this is that the rough wall on top of the step hinders the flow to form a recirculation bubble due to high irregular peaks of the roughness elements. A similar observation was reported in the study of Ren and Wu, 2013. The upstream smooth wall has higher momentum fluid compared to the larger momentum deficit flow over rough walls, and as a consequence, the deflected shear layer over rough walls accelerates more gradually compared to the smooth wall. For example, the maximum velocity for SM-SM case in the vicinity of the leading edge of the step, $U_{max}/U_e \approx 1.19$ occurs at $(x/h, y/h) = (0.68, 1.56)$ whereas for SP-SM case, the maximum velocity $U_{max}/U_e \approx 1.12$ occurs at (0.63, 1.54) and for SG-SM case $U_{max}/U_e \approx 1.11$ it occurs at (0.53, 1.51). These locations are in good agreement with the locations reported by Essel et al., 2015. The magnitude of maximum backflow within the primary recirculation bubble was $0.13U_e$ for SM-SM, $0.16U_e$ for SP-SM and $0.19U_e$ for SG-SM which compared well with $0.15U_e$ to $0.36U_e$ reported in previous studies (Sherry et al., 2010; Hattori and Nagano, 2010). The SP-SP case did not show any reverse flow as there was no distinct recirculation bubble.

4.2.2 The reattachment length

The recirculation bubble, enclosed by the zero mean velocity contour line, exhibited different physical sizes for the smooth and rough cases. Upstream roughness and its inherent enhanced turbulence level influenced the recirculation bubble by reducing the physical size of the bubble both in streamwise and wall-normal extents. The streamwise extent of the bubble or the reattachment length L_r was estimated using three techniques: (i) the zero mean velocity on the downstream wall, (ii) streamwise location of mean dividing streamline and (3) 50% forward flow fraction. The variations in reattachment point for a particular test condition for the three aforementioned methods are comparable to measurement uncertainty of $\pm 0.05h$ and as a result the average values were used in the present study. The reattachment length, L_r/h and the wall-normal extent of the bubble, H_r/h for SM-SM is respectively 1.78 and 0.16. Upstream roughness decreased the reattachment length and the wall-normal extent of the bubble. For example, Lr/h and H_r/h are 1.53 and 0.12, respectively for SP-SM and 1.26 and 0.09 respectively for SG-SM.

The reattachment length for the smooth wall in the present study is 59% shorter than the value reported by Sherry et al., 2010 at a comparable Reynolds number; however, it compares well with the value obtained by Essel et al., 2015 at a slightly higher Reynolds number (Re_h = 4030). Essel et al., 2015 argued that the difference between the L_r for the upstream smooth wall in their study and previous smooth wall studies is likely due to the relatively higher background turbulence levels and blockage ratio which is also the case in the present study. One should recall that Kiya and Sasaki, 1983 observed a monotonic decrease of L_r/h from 10 to 3 by increasing the turbulence levels by 6%, although they

used blunt plate and a different approach to generate the higher turbulence levels than in the present study.

A reduction of the reattachment length by the upstream roughness was also observed in previous studies. Essel et al., 2015 obtained similar L_r/h using sand grain as the roughness element. The larger turbulence scales generated by the upstream rough walls produced efficient turbulent mixing and entrainment of outer high speed fluid which in turn reduced the reattachment length.

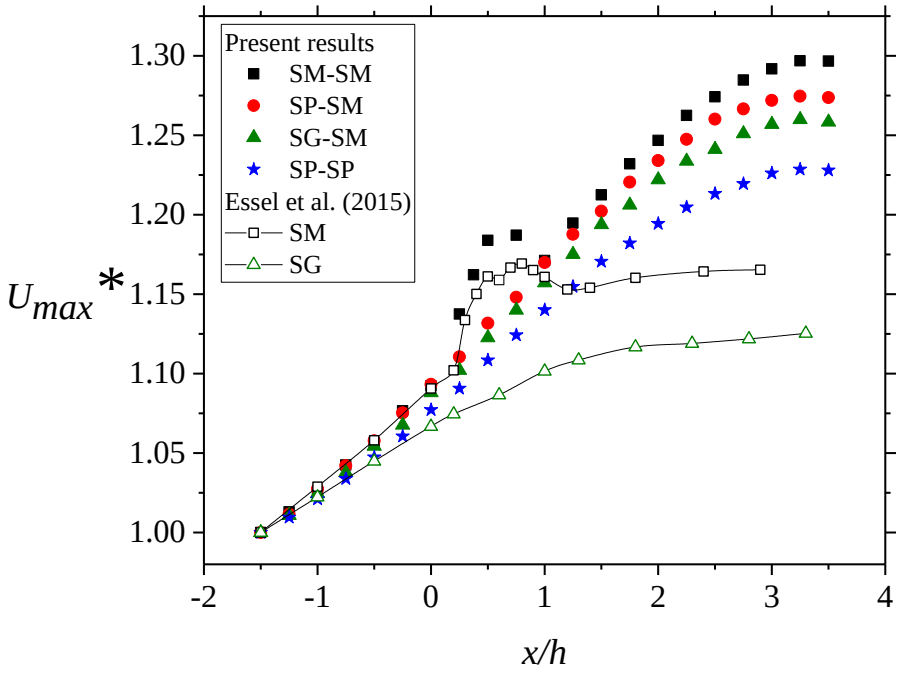

Figure 4.3 Maximum streamwise mean velocities at the leading edge of the step for different wall conditions.

4.2.3 Local maximum streamwise mean velocity

The influence of upstream and downstream wall roughness on flow acceleration over the step is examined in Figure 4.3. The distribution of local maximum streamwise velocity

with streamwise distance near the leading edge of the step is shown in this figure. The datasets from Essel et al., 2015 at comparable Reynolds numbers are also shown for comparison. The local maximum streamwise mean velocity, U_{max} is normalized as follows, $U_{max}* = U_{max}/U_{max@-1.5}$, where $U_{max@-1.5}$ is the local maximum velocity at x/h = -1.5. The streamwise mean freestream velocity, U_e was not used to normalize the local maximum velocities, firstly because U_e failed to show good agreement and consistent trend among different datasets over different wall conditions; and secondly, to facilitate comparison of the present results with those reported by Essel et al., 2015. For the smooth upstream, U_{max}* increased from 1.09 at separation point to a local peak value of 1.19 at x/h = 0.75. This was followed by a sudden deceleration to 1.17, and then the flow started to accelerate towards an asymptotic value of U_{max}* = 1.30 at x/h = 3. For the rough cases, the acceleration was much slower compared to the smooth wall which is an artifact of the larger momentum deficit caused by the rough walls. No distinct local peak was observed for the upstream roughness (SP-SM, SG-SM and SP-SP). The rough cases also reached asymptotic values at x/h = 3 but the increase towards the respective asymptotic value is more gradual than observed for the upstream smooth case (SM-SM). Furthermore, the asymptotic values for SP-SM, SG-SM and SP-SP are respectively 2.4%, 3.2% and 5.7% lower than the corresponding value observed for SM-SM. As shown in Figure 4.3, Essel et al., 2015 observed a similar acceleration trend in their upstream smooth (SM) and upstream rough (SG) experiments; however, the asymptotic values in the present study are significantly higher than reported in the previous experiments.

4.2.4 Wall-normal mean velocity

The wall-normal mean velocity contour plots are shown in Figure 4.4. The flow is deflected at the leading edge of the step, producing high positive wall-normal mean velocity. This region is consistent with the upward transport of low momentum fluid into the outer high speed flow. On the other hand, the region of negative wall-normal velocity signifies entrainment of high momentum fluid from the outer flow to replenish low momentum region close to the step. The interface between the upward transport of low momentum fluid and downward transport of high momentum fluid is demarcated by the zero wall-normal mean velocity contour level. The streamwise location where the zero contour level emerges from the step closely matches the centre of the recirculation bubble for respective cases. The positive wall-normal velocities in the vicinity of the leading edge of the step are relatively higher for the upstream smooth wall (about $0.55U_e$) in comparison to the rough walls (about $0.50U_e$). This shows that the ability of the separated shear layer to permeate into the outer high-speed fluid is weakened by the upstream rough wall itself. Although the negative wall-normal velocities are an order of magnitude lower than the positive values, they are nonetheless non-negligible. These high wall-normal velocities are responsible for significant transport of momentum and turbulence.

4.2.5 Reynolds shear stress

Figure 4.5 shows the contour plots of Reynolds shear stress ($-\overline{u'v'}$) in the recirculation and reattachment regions. In the immediate vicinity of the leading edge of the step,

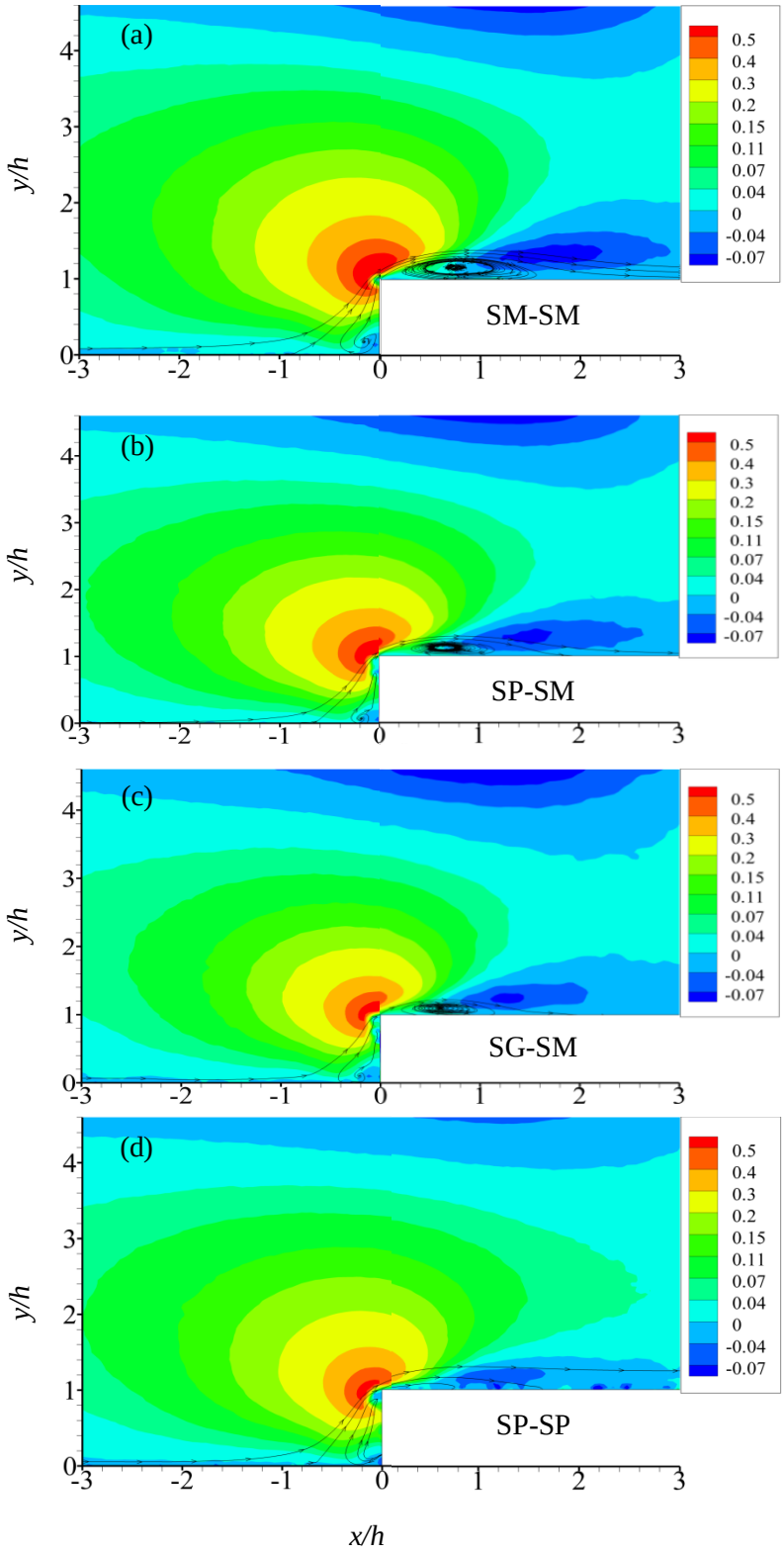

Figure 4.4 Contour plots of wall-normal mean velocity in the recirculation region.

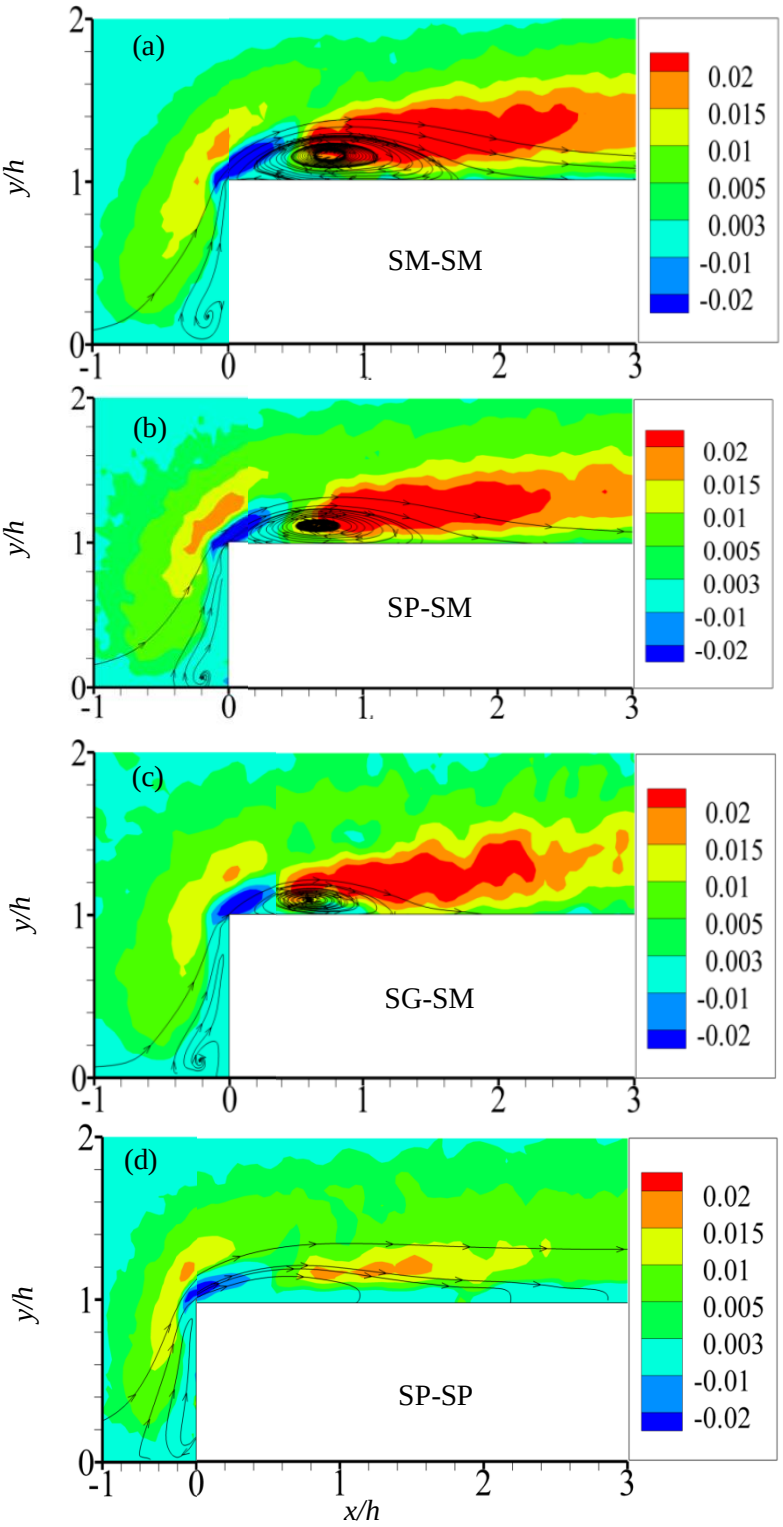

Figure 4.5 Contour plots of Reynolds shear stress in the recirculation region

maximum negative $-\overline{u'v'}$ can be observed and after about one step height from the leading edge of the step, a maximum positive $-\overline{u'v'}$ is observed for all the test condition. It is important to note that the locations of the maximum negative and positive $-\overline{u'v'}$ coincide with the locations of positive and negative wall-normal mean velocity which correspond to the transport of low and high momentum fluid upward and toward the wall respectively. The magnitude of the maximum negative $-\overline{u'v'}$ is 0.02, which is similar to the magnitude of the maximum positive $-\overline{u'v'}$ for SM-SM, SP-SM and SG-SM. However, the positive peak for SP-SP is 33% lower than the negative peak, implying that the maximum peak was reduced by wall roughness on top of the step. The presence of wall roughness on top of the step makes the size of the maximum positive $-\overline{u'v'}$ contour level of SP-SP smaller and more flat in comparison to when the step is smooth (SM-SM, SP-SM and SG-SM). The occurrence of negative and positive peaks respectively in the immediate vicinity of the leading edge of the step and further downstream was also observed in previous studies (Essel et al., 2015, Ren and Wu, 2011).

4.2.6 Mean velocity profiles

One dimensional profiles of streamwise mean velocity *U* and wall-normal mean velocity *V* in the recirculation bubble and reattachment region are shown in Figure 4.6 (a, b). The profiles were obtained at selected streamwise locations, *x/h* = 0, 0.5, 1, 2 and 3 to quantify the effect of upstream and downstream wall roughness inside the recirculation region and in the early recovery region. The local maximum velocity U_m was used as the velocity scale for each streamwise location. Figure 4.6 (a) demonstrates that upstream

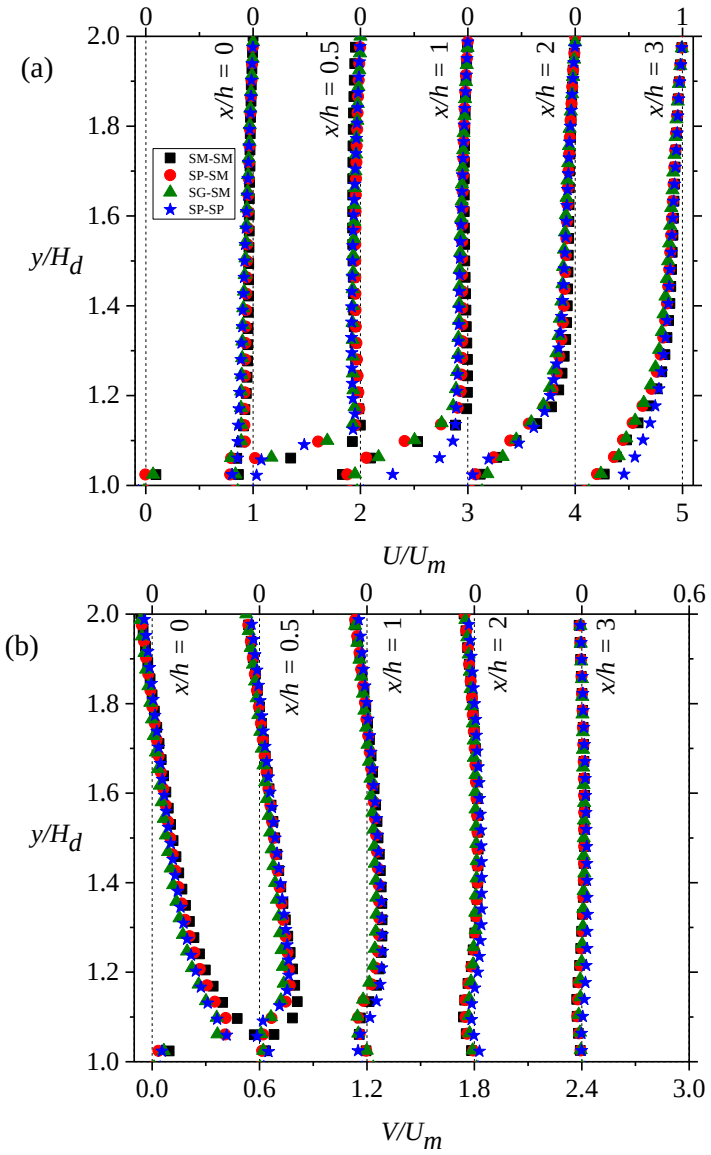

Figure 4.6 Profiles of (a) streamwise mean velocity and (b) wall-normal mean velocity in the recirculation region.

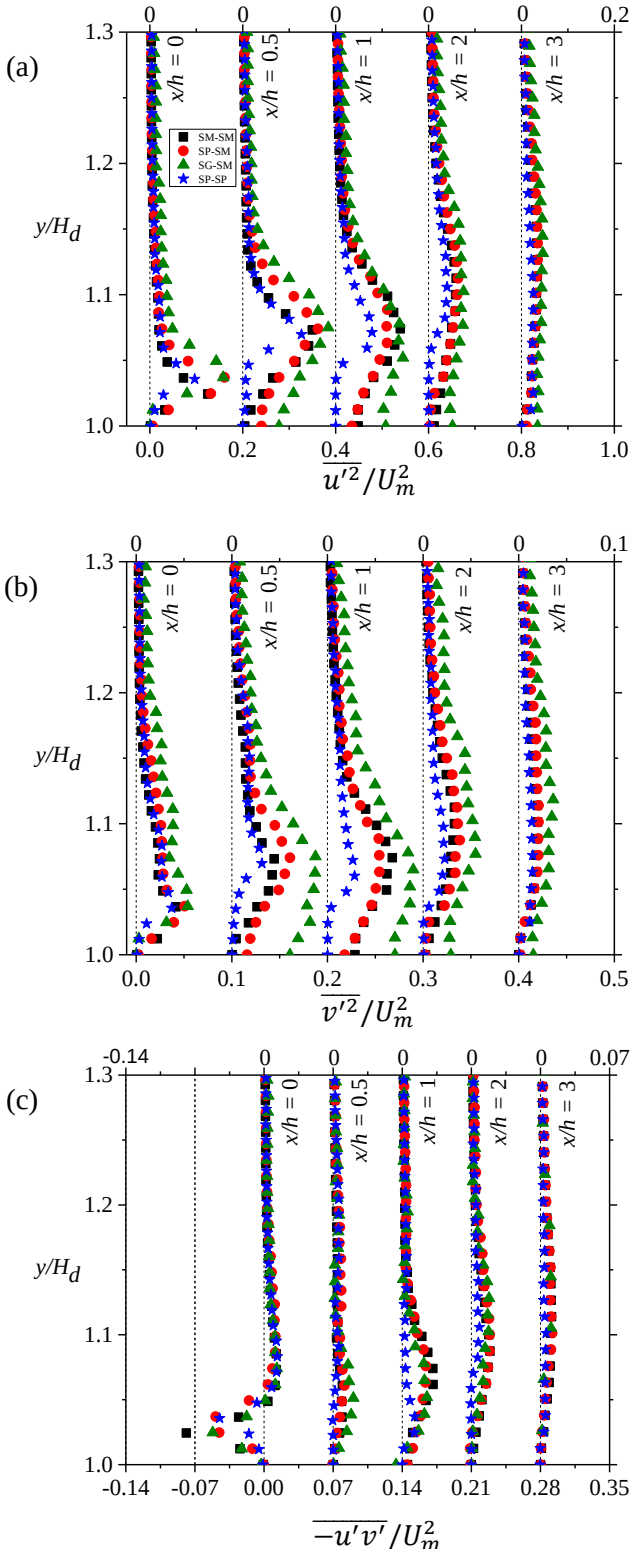

Figure 4.7 Profiles of (a) streamwise Reynolds normal stress, (b) wall normal Reynolds normal stress and (c) Reynolds shear stress in the recirculation region.

wall roughness has no significant effect on the streamwise mean velocity within the separated and reattached region. On the other hand, the downstream roughness showed significant effect on the streamwise mean velocity immediately after the reattachment. It gradually reduces the streamwise mean velocity as the flow develops downstream. Similar to what was observed in the contour plots, negative velocities or backflows were observed in the cases of SM-SM, SP-SM and SG-SM. Since there was no recirculation bubble for SP-SP case, no negative velocities were observed.

The profiles of wall-normal mean velocity are shown in Figure 4.6 (b). The profiles at the separation (x/h = 0) are positive, and the SM-SM case showed the strongest positive flow compared to other three cases at this location. For example, the maximum positive peak of SM-SM was about 36% higher than the rough cases. As the flow develops downstream, the peak values decreased and became negative due to entrainment and mixing. The reduction in wall-normal mean velocity with streamwise distance is more rapid for the smooth case compared to rough cases.

4.2.7 Profiles of Reynolds stresses

Profiles of Reynolds stresses at the selected streamwise locations in the recirculation and reattachment regions over smooth and rough walls are presented in Figure 4.7. Figure 4.7 shows the profiles of streamwise Reynolds normal stress ($\overline{u'^2}/U_e^2$), wall normal Reynolds normal stress ($\overline{v'^2}/U_e^2$) and Reynolds shear stress ($-\overline{u'v'}/U_e^2$). Inside the recirculation bubble (x/h = 0.5) and near the reattachment (x/h = 1), the peak values observed for $\overline{u'^2}/U_e^2$ for all the wall conditions are an order of magnitude higher than the corresponding upstream values. The higher $\overline{u'^2}/U_e^2$ observed in the recirculation region is

not produced by the upstream wall condition *per se*, but by the large eddies associated with the separation process. Similar observation was made in Essel et al., 2015. The wall-normal Reynolds normal stress and Reynolds shear stress showed two distinct regions of higher peaks for all the wall conditions (Figure 4.7 (b) and (c)). The first region, which is located close to the leading edge of the step, coincides with the region of large positive wall-normal velocity shown in contour plots (Figure 4.4). This region is associated with the upward transport of low momentum fluid into outer high-speed flow. In this region, wall-normal Reynolds normal stress showed a positive peak and Reynolds shear stress showed a negative peak ($\overline{v'^2}/U_e^2$ = 0.042; $-\overline{u'v'}/U_e^2$ = 0.078 for smooth wall). The second region is located near the reattachment and coincides with the region of negative wall-normal mean velocities corresponding to the transport of high momentum fluid towards the wall (Figure 4.4).

Close to the leading edge of the step, upstream roughness increased $\overline{u'^2}$ and v'^2 but $-\overline{u'v'}$ was nearly independent of upstream wall condition. Furthermore, SP-SM and SG-SM both showed a 26% higher peak of $\overline{u'^2}/U_e^2$ compared to SM-SM. Similarly, the maximum peaks of $\overline{v'^2}/U_e^2$ for SP-SM and SG-SM were almost 29% higher than the corresponding peak for SM-SM. The peaks of the Reynolds stresses for SP-SP were lower compared to the other wall conditions. As the shear layer develops, both the streamwise and wall-normal Reynolds stresses start decaying and at x/h = 3 all the profiles are nearly independent of upstream wall condition. The gradual reduction and spreading of the stresses with the streamwise distance are associated with the breakdown of large scale structures generated from separation.

4.2.8 Turbulence kinetic energy

The one dimensional profiles of turbulent kinetic energy (k) in the separated and reattached region over smooth and rough walls are presented in this section. The turbulent kinetic energy is given by

$$k = 0.5(\overline{u'^2} + \overline{v'^2} + \overline{w'^2}) \tag{4.1}$$

Since the spanwise Reynolds normal stress ($\overline{w'^2}$) was not possible to measure in the present study, it was approximated as 0.5 ($\overline{u'^2} + \overline{v'^2}$). The profiles of turbulent kinetic energy are presented in Figure 4.8. Inside the recirculation bubble (x/h = 0.5), wall roughness effects are significant. At this location, the peak values of turbulent kinetic energy for SG-SM and SP-SM are respectively 14% and 5% higher than the corresponding value over smooth wall (SM-SM). On the other hand, the peak value for SP-SP is 14% lower than the smooth wall value. The higher turbulent kinetic energy in the SG-SM case may be attributed to the relatively larger average roughness height. It should be recalled that the average roughness height k_t of SG is approximately 40% larger than that of SP. Furthermore, it was observed in Section 4.2.6 that wall roughness increased the wall-normal Reynolds normal stress more than the streamwise Reynolds normal stress. This conclusion is also consistent with previous studies performed to investigate wall roughness effects in canonical wall-bounded shear flows (Krostad et al., 1999).

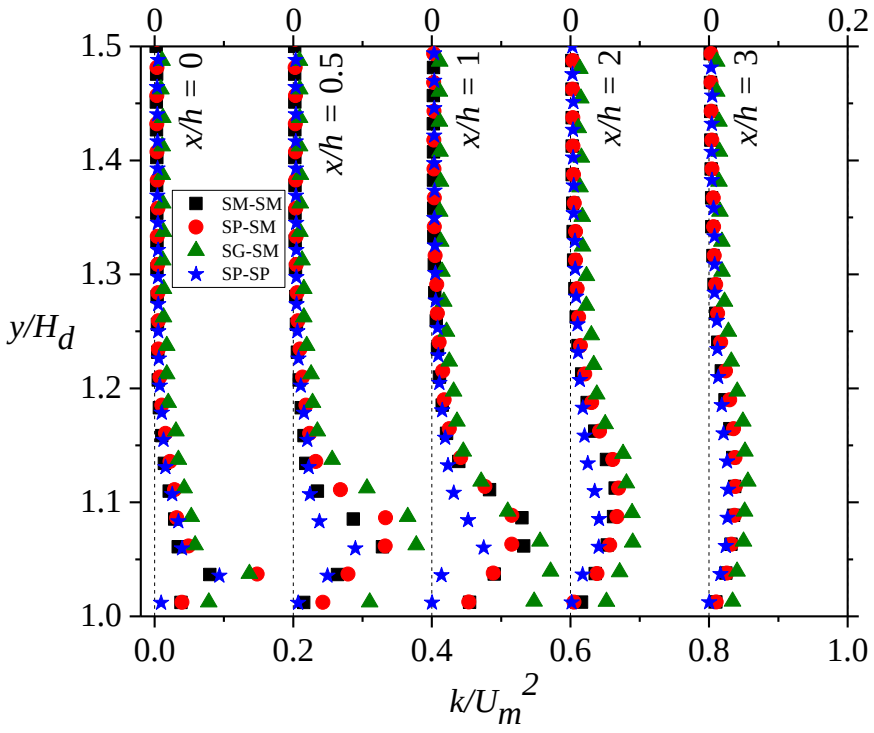

Figure 4.8 Profiles of turbulent kinetic energy in the recirculation region

4.3 Recovery region

The flow characteristics in the recovery region and the development of the new boundary layer are presented in this section. This section is divided into three sub-sections. In the first section, wall roughness effects on the mean velocities and turbulent quantities such as streamwise and wall-normal Reynolds stresses and Reynolds shear stress are discussed. In the second section, the integral parameters such as shape factor, skin-friction coefficient and Clauser shape parameter are used to quantify the effects of wall roughness on the recovery of the boundary layer downstream of reattachment. The third

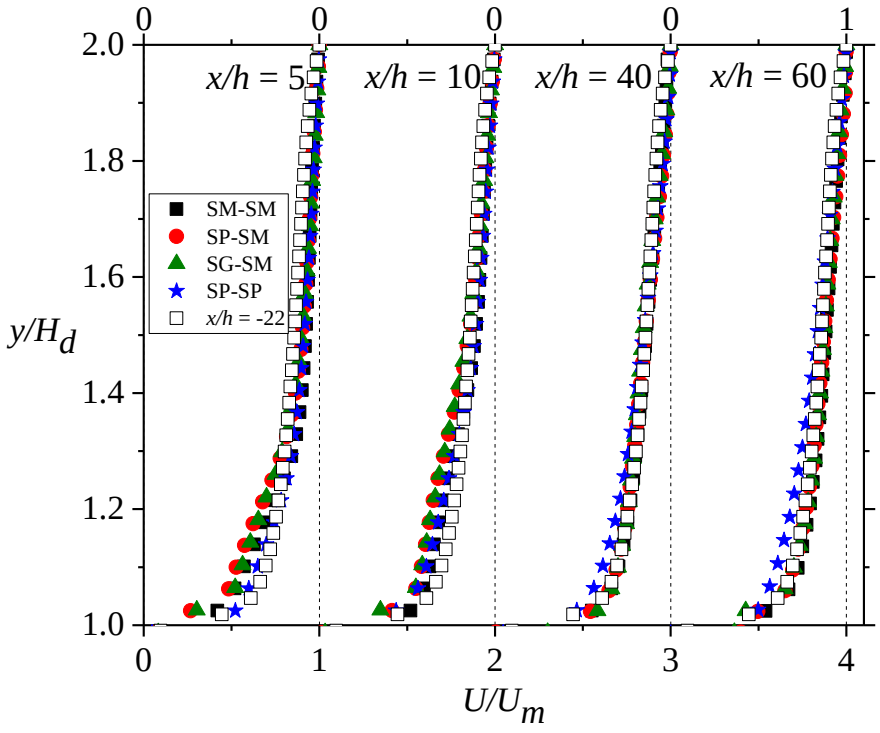

Figure 4.9 (a) Profiles of streamwise mean velocity in outer coordinates of the recovery region.

section examines the coherent structures embedded in the flow using two-point auto correlation function. It should be noted that the appropriate scaling in the inner region of the boundary layer is the friction velocity (U_τ) and viscous length scale (ν/U_τ) whereas the outer region of the boundary layer is scaled on the freestream velocity (U_e) and the boundary layer thickness (δ). In this study, the local maximum freestream velocity (U_m) and the step height (h) were adopted in preference over δ to scale the quantities in the recovery region. This helped to facilitate interpretation of the inner region of the boundary layer in terms of step height.

4.3.1 Recovery of mean velocity and turbulent quantities

The recovery of the mean and turbulent quantities after the reattachment is examined in Figure 4.9. Profiles of streamwise mean velocity, Reynolds normal and shear stresses

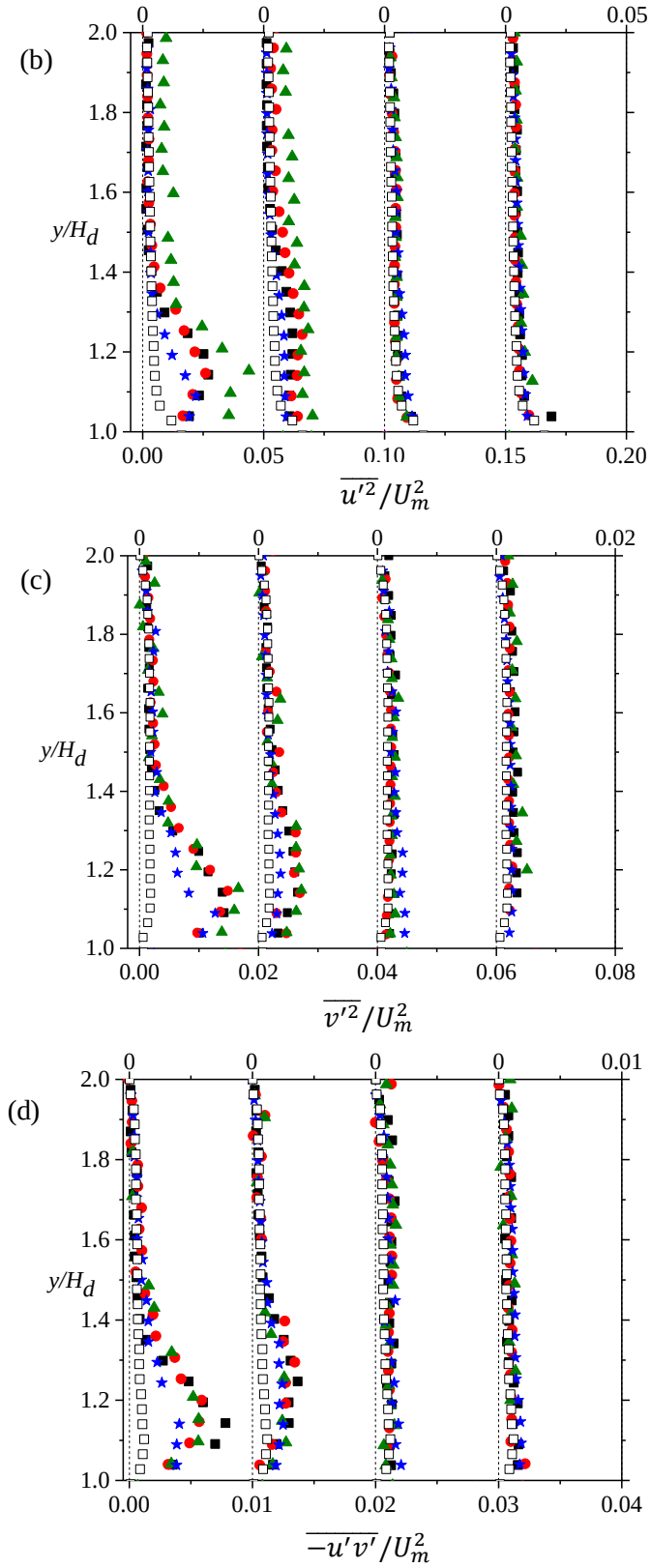

Figure 4.9 Profiles of (b) streamwise Reynolds normal stress, (c) wall-normal Reynolds normal stress and (d) Reynolds shear stress in outer coordinates of the recovery region.

within the recovery region in outer coordinates are compared with the corresponding smooth upstream profiles at *x/h* = -22. These profiles were obtained at selected streamwise locations, *x/h* = 5, 10, 40 and 60. In the early recovery region (*x/h* = 5), from Figure 4.9 it can be seen that all the profiles greatly varied compared to the smooth upstream profile. As the flow develops downstream, the disparity between the upstream and downstream profiles diminishes and the downstream profiles gradually collapse on to the upstream smooth profile. The effect of upstream roughness on streamwise mean velocity is not significant after *x/h* = 40, but the effect of downstream roughness starts to emerge. It is evident from Figure 4.9 (a) that at the last measurement location, *x/h* =60, the mean velocity profiles for SM-SM, SP-SM and SG-SM collapse reasonably well on to the upstream profile, however, profile of SP-SP showed a reduced mean velocity. This disparity persists up to y/H_d = 1.5, beyond which the differences in values are within measurement uncertainty. This phenomenon is an artifact of the rough wall turbulent boundary layer as it reduces the mean velocity close to the wall due to higher drag and was also observed in previous rough wall turbulent boundary layer and FFS studies (Tachie et al., 2003; Shao and Agelinchaab, 2016).

The profiles of streamwise Reynolds normal stress, wall-normal Reynolds normal stress and Reynolds shear stress in outer coordinates are shown in Figure 4.9 (b), (c) and (d) respectively. In the early recovery region, *x/h* = 5, the Reynolds normal stresses and Reynolds shear stress for all the test cases are higher than the respective upstream profiles from wall up to y/H_d = 1.5. As the flow evolves downstream, the profiles of $\overline{u'^2}$, $\overline{v'^2}$and $-\overline{u'v'}$ decay closer to the upstream values at *x/h* = 40. The $\overline{u'^2}$ profiles converge towards the upstream profile faster than $\overline{v'^2}$ and $-\overline{u'v'}$. The results showed that at the last

measurement location, x/h = 60, the profiles do not completely collapse on to the upstream profiles which means the Reynolds stresses require longer streamwise distance to completely collapse on to the upstream profiles than required for the mean velocity. This slower recovery or relaxation process of the Reynolds stresses have been reported in several previous studies (Castro and Epik, 1996; Tachie et al., 2001; Essel and Tachie, 2015; Shao and Agelinchaab, 2016). For example, in the recent study by Shao and Agelinchaab, 2016, the profiles of streamwise turbulence intensity and Reynolds shear stress did not collapse on to the upstream profiles at x/h = 60. Moreover, Tachie et al., 2001 did not observe self-similarity in the turbulence intensity at $x/h < 100$.

4.3.2 Recovery of integral parameters

The distributions of shape factor H, skin friction coefficient C_f and Clauser shape parameter G, shown in Figure 4.10, are also used to quantify the recovery of boundary layer downstream of reattachment. The upstream values of each of these parameters are indicated on the right side of each figure with an arrow. The parameters were obtained at selected streamwise locations from the reattachment at x/h =1 to the last measurement location at x/h = 60. The values of the boundary layer shape factor, H increased considerably in the region immediately downstream of reattachment (Figure 4.10 (a)). These relatively higher values of H are an indication of departure of the boundary layer from the upstream reference. H recovers towards the upstream values after $x/h \geq 20$. At x/h = 40 and beyond, the difference in values of H for all the cases compared to the corresponding upstream values is comparable to the measurement uncertainty.

The skin friction coefficient, C_f was estimated using the Ludwieg-Tillman formula:

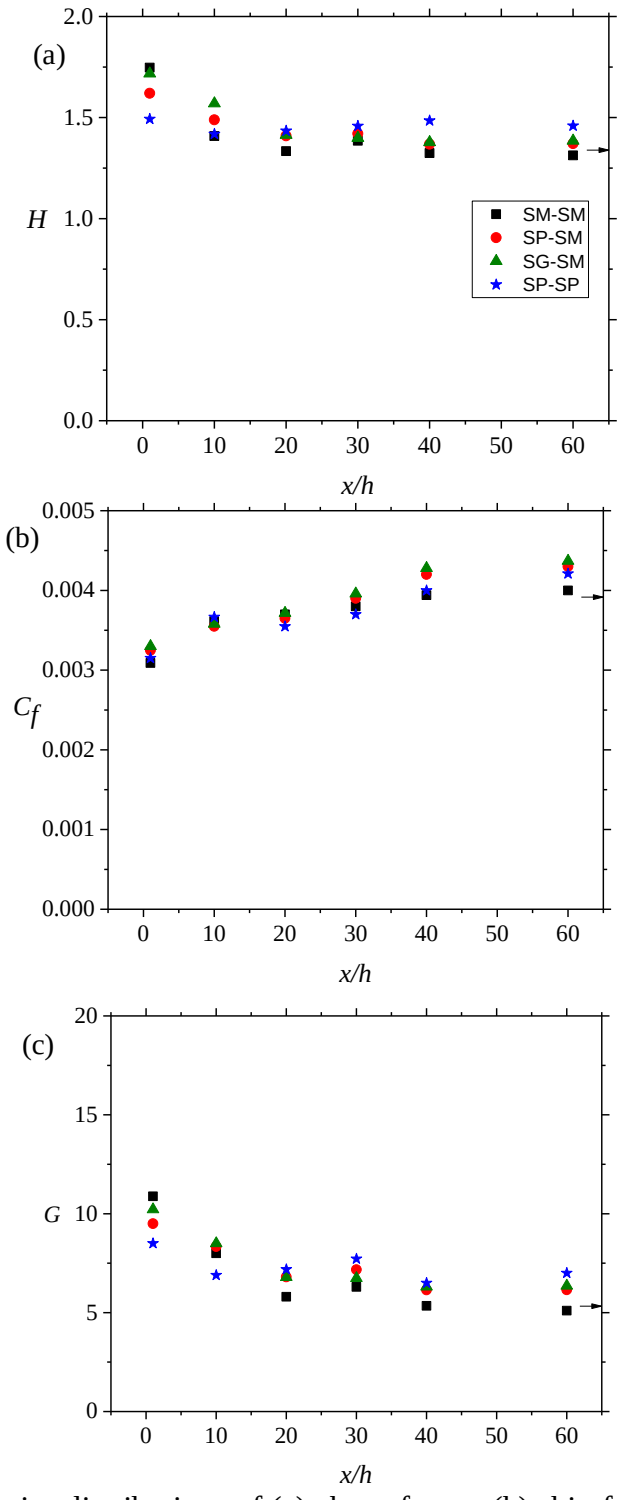

Figure 4.10 Streamwise distributions of (a) shape factor, (b) skin friction coefficient and (c) Clauser shape parameter in the recovery region.

$$C_f = 0.246 \times 10^{-0.678H} \times {Re_\theta}^{-0.268} \quad (2)$$

It should be noted that this formula has been used in previous separated and reattached flows successfully and the maximum variation from the skin friction values determined from direct measurements of the shear stress was found to be less than 10% (Bradshaw and Wong, 1972). Unlike the upstream region, the conventional approach for estimating C_f, the Clauser plot method, was not used here because it could give an inaccurate estimation of C_f because of the presence of strong APG in this region (Essel and Tachie, 2015). After the reattachment, lower values of C_f were observed compared to the upstream, similar observation was reported by Essel and Tachie, 2015 and this is attributed to the APG effects. The values of C_f increased as the flow evolves downstream for all the test conditions and gradual recovery towards the upstream value was observed. The C_f values reached an asymptotic value at x/h = 40, and the distribution of C_f is independent of the upstream roughness.

The Clauser shape parameter, G is shown in Figure 4.10(c). It should be noted that the Clauser parameter is a benchmark for estimating the relaxation of a shear flow to its equilibrium state (Bradshaw and Wong, 1972). The Clauser shape parameter was determined using the following formula:

$$G = \left(\frac{2}{C_f}\right)^{0.5} \times \frac{H-1}{H} \quad (3)$$

Similar to H, the Clauser shape parameter increases immediately after the reattachment and then slowly recovers to the upstream value after x/h = 20. The shape parameter reached an asymptotic value at x/h = 40 and persists to the last measurement location, x/h

= 60. The distribution of G is also independent of the upstream roughness. Similar trends of *H* and *G* have been reported previously by Tachie et al., 2001 and Balachandar and Tachie, 2001. Based on these results, it was concluded that the inner and outer layers of the boundary layer downstream of the reattachment recover reasonably well at *x/h* = 40 irrespective of the upstream and downstream wall conditions.

4.3.3 Turbulent production

The contributions of the individual terms in the production term of the turbulent kinetic energy transport equation are examined in the recirculation and recovery regions. The production term in the transport equation of turbulent kinetic energy was estimated as follows: $P_k = -(\overline{u'^2}\frac{\partial U}{\partial x} + \overline{v'^2}\frac{\partial V}{\partial y} + \overline{u'v'}(\frac{\partial U}{\partial y} + \frac{\partial V}{\partial x}))$. This can be decomposed into contributions from normal stresses, $P_n = -(\overline{u'^2}\frac{\partial U}{\partial x} + \overline{v'^2}\frac{\partial V}{\partial y})$ and contributions from shear stresses, $P_s = -\overline{u'v'}(\frac{\partial U}{\partial y} + \frac{\partial V}{\partial x})$. The profiles of the individual terms and the total production term at selected streamwise location in the recirculation region (*x/h* = 0, 0.5 and 1) and redevelopment region (*x/h* = 10, 40 and 60) over SM-SM are shown in Figure 4.11. The results for the rough cases were observed to be qualitatively similar. The production terms were normalized using (U_m^3/h). Figure 4.11 (a) demonstrates that the major contributor to the turbulent production in the recirculation region is $-\overline{u'v'}\frac{\partial U}{\partial y}$ while $\overline{-u'v'}\frac{\partial V}{\partial x}$ does not make any significant contribution. Although the individual contributions from $-\overline{u'^2}\frac{\partial U}{\partial x}$ and $\overline{-v'^2}\frac{\partial V}{\partial y}$ are not negligible, they are of similar magnitude but opposite sign so that their sum is insignificant compared to the contributions from $-\overline{u'v'}\frac{\partial U}{\partial y}$. It can be observed from Figure 4.11 (b) that the contributions from $-\overline{u'^2}\frac{\partial U}{\partial x}$,

$\overline{-v'^2}\frac{\partial V}{\partial y}$ and $\overline{-u'v'}\frac{\partial V}{\partial x}$ at the later stage of flow recovery are negligible or nearly zero thus $-\overline{u'v'}\frac{\partial U}{\partial y}$ is responsible for virtually the entire production of turbulence.

The contour plots of P_n^*, P_s^* and $-\overline{u'v'}\frac{\partial U}{\partial y}$ over SM-SM in the recirculation region are examined in Figure 4.12 in order to obtain qualitative information about turbulent production in that region. The P_n^* contours revealed a region of high negative values of total production of turbulence kinetic energy close to the leading edge of the step. The negative values suggest that the contributions from the normal stresses act as an "energy sink". The region of negative production in the P_s^* contour was produced from a strong negative $-\overline{u'v'}$ combined with a strong positive $\frac{\partial U}{\partial y}$. Immediately downstream of the leading edge, the contributions from the normal stresses become positive and this, together with the positive production from the shear stress, is responsible for the net positive production of turbulent kinetic energy on the step.

The effect of roughness on turbulence production was examined using contour plots of total production term of turbulent kinetic energy, P_k^* over the smooth and rough walls in the recirculation region and are shown in Figure 4.13. It can be observed that the positive peak occurred at about a step height downstream from the leading edge of the step for all the wall conditions. Moreover, the rough upstream walls seemed to suppress the turbulent kinetic energy production in the recirculation region compared to the smooth upstream wall. For example, positive peak value of SM-SM was 4.5%, 27% and 50% larger than the positive peak values for SP-SM, SG-SM and SP-SP respectively. Similar observations were reported in the recirculation region in the study of Shao and

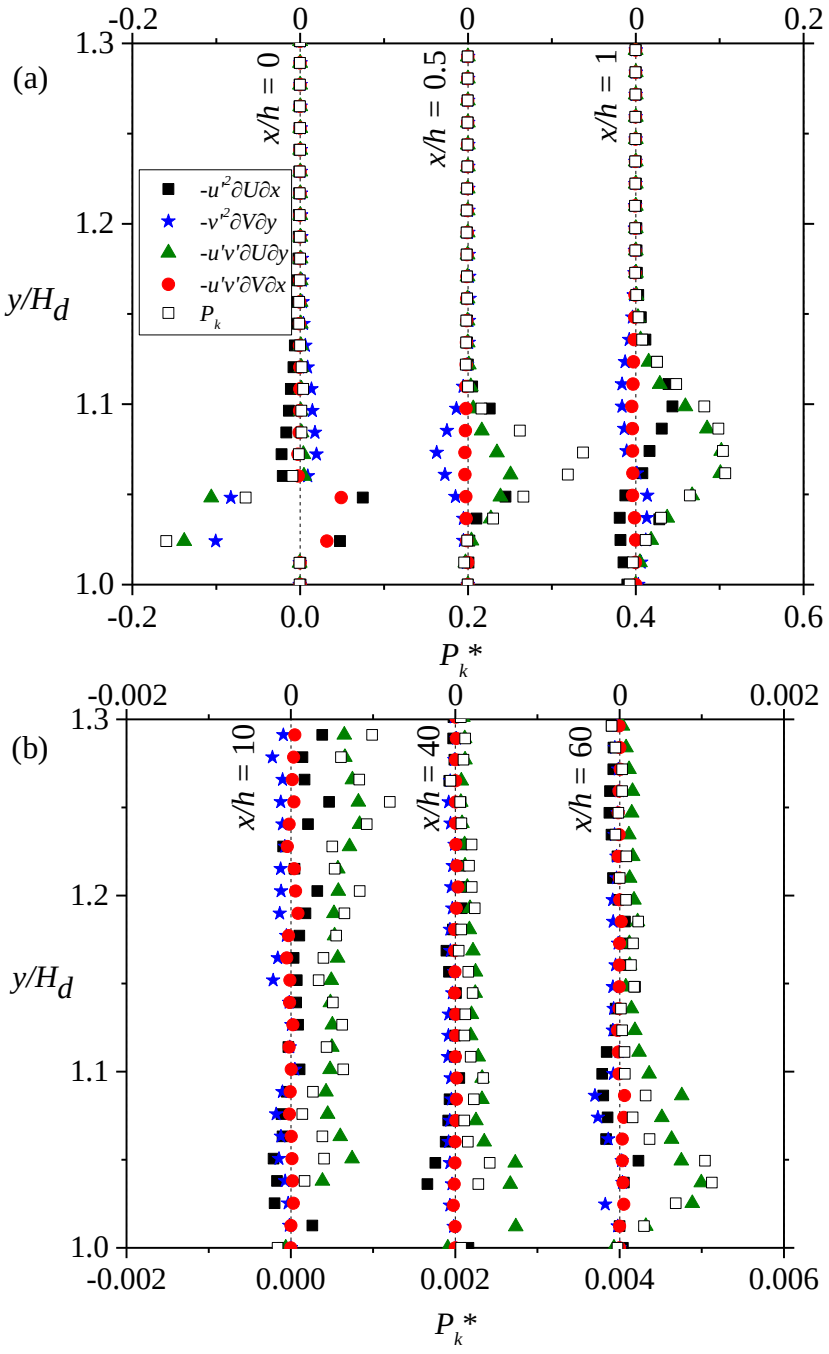

Figure 4.11 Profiles of the individual terms of the total production term of the transport equation of turbulent kinetic energy (P_k*) in the (a) recirculation region and (b) redevelopment region over smooth wall (SM-SM).

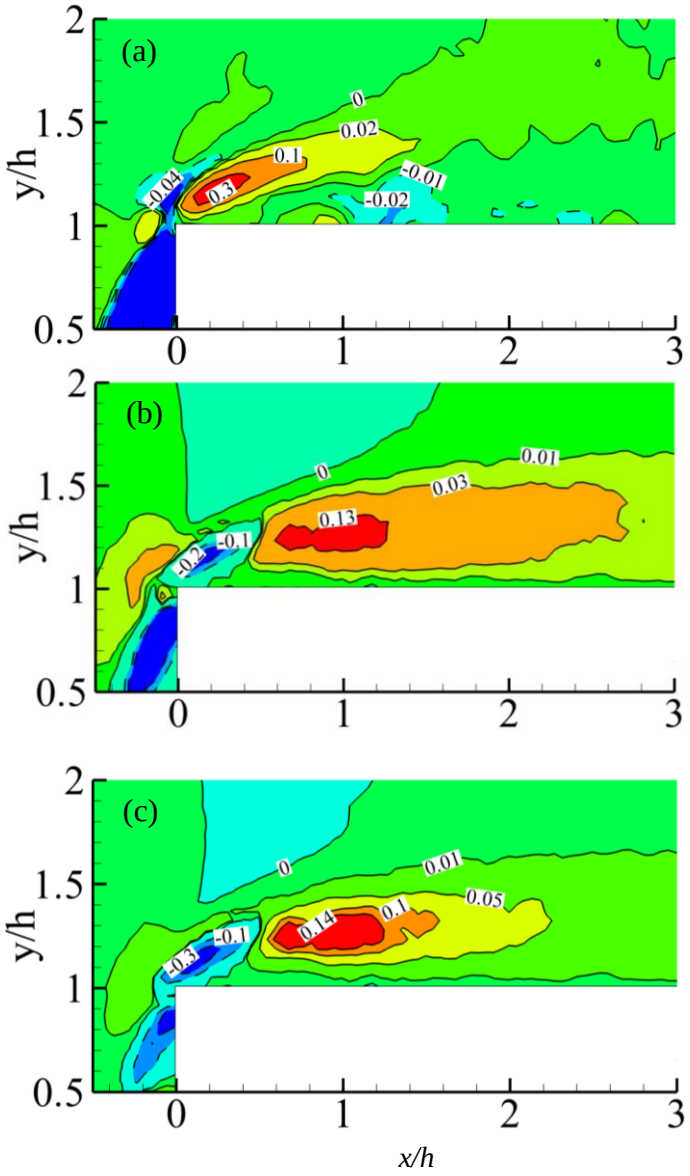

Figure 4.12 Contour plots of dimensionless (a) P_n^*, (b) P_s^* and (c) $-\overline{u'v'}\frac{\partial U}{\partial y}$ production terms in the recirculation regions over SM-SM.

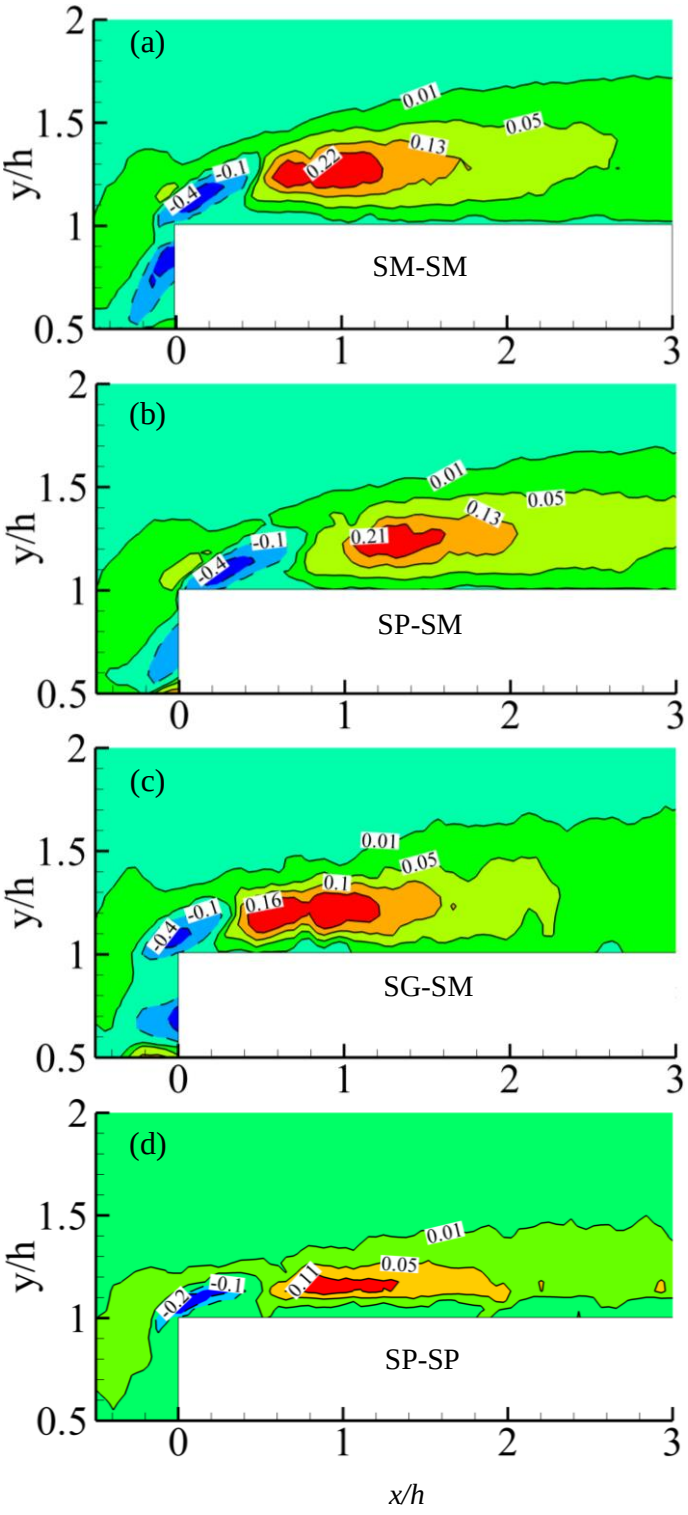

Figure 4.13 Contour plots of dimensionless production term of turbulent kinetic energy transport equation, P_k^* in the recirculation region over (a) SM-SM, (b) SP-SM, (c) SG-SM and (d) SP-SP.

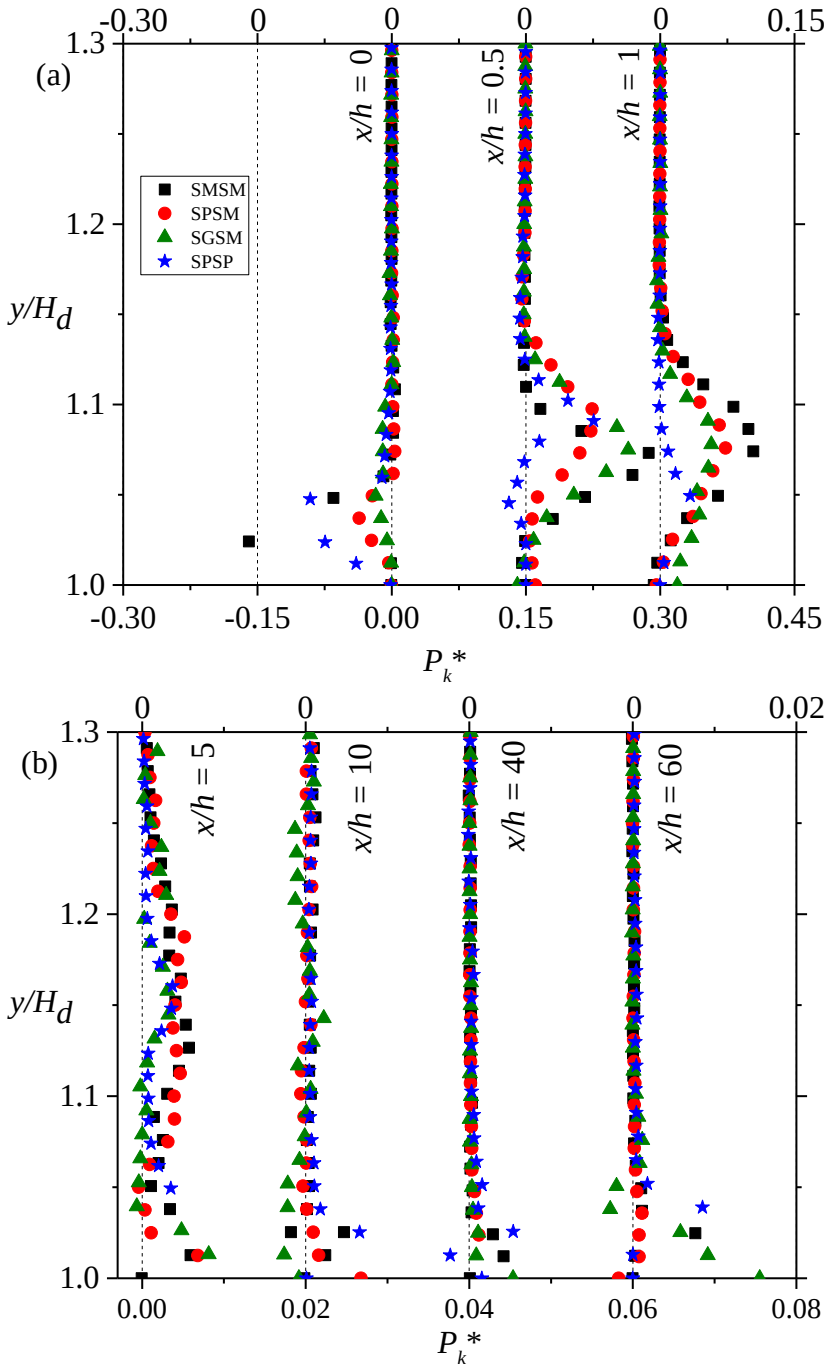

Figure 4.14 Profiles of dimensionless turbulent production of the transport equation of turbulent kinetic energy (P_k*) in the (a) recirculation region and (b) redevelopment region over all wall conditions.

Agelinchaab, 2016. On the other hand, the downstream rough wall of SP-SP suppressed the production of negative peak by 50% compared to the other three cases.

The distributions of the total turbulent production in the recirculation and redevelopment regions over all wall conditions are compared in Figure 4.14. Similar to the contour plots, the total production of turbulent kinetic energy is significantly larger in the recirculation region than it is in the farther downstream of reattachment. Roughness suppressed the turbulent kinetic energy production in the recirculation region. SG-SM showed 8% decrease in the production of turbulent kinetic energy compared to SM-SM while SP-SM and SP-SP both showed a 28% decrease. However, no significant wall roughness effect was observed in the recovery region.

4.3.3 Two point correlation analysis

Two-point correlation functions were used to quantify the effects of upstream and downstream roughness on the coherent structures and the spatial extent of the integral scales in the recovery regions. The two-point auto correlation function (R_{AB}) is defined as follows:

$$R_{AB}(x_{ref} + \Delta x, y_{ref} + \Delta y) = \frac{A(x_{ref}, y_{ref})B(x_{ref} + \Delta x, y_{ref} + \Delta y)}{\sigma_A(x_{ref}, y_{ref})\sigma_B(x_{ref} + \Delta x, y_{ref} + \Delta y)} \quad (4)$$

where x_{ref} and y_{ref} indicate the streamwise and wall-normal reference location respectively, A and B are the fluctuating velocity components, Δx and Δy are the spatial separation in the streamwise and wall-normal directions between A and B respectively and σ_A and σ_B are the root-mean-square values of A and B at (x_{ref}, y_{ref}) and ($x_{ref} + \Delta x$, $y_{ref} + \Delta y$) respectively. The two-point correlation functions were calculated for each PIV realization and then ensemble-averaged point by point.

Contours of streamwise (R_{uu}) and wall-normal (R_{vv}) auto-correlations were obtained at the reattachment point, and the recovery region to examine how the structures evolve downstream. The contours were centered at two different wall-normal locations above the step wall at y/h = 1.25 and 2. The contour levels varied from 0.5 to 0.9 at an interval of 0.1. The dashed lines, representing the streamwise and wall-normal locations, intersect at the self-correlation point. The contours of streamwise (R_{uu}) and wall-normal (R_{vv}) auto-correlations at the reattachment point (x/h =1) at y/h =1.25 and 2 are shown in Figure 4.15 and 4.16 respectively. The R_{uu} contours have elongated shape in the streamwise direction which suggests that the embodied structures are more correlated in the streamwise direction than in the wall-normal direction. The R_{vv} contours are more

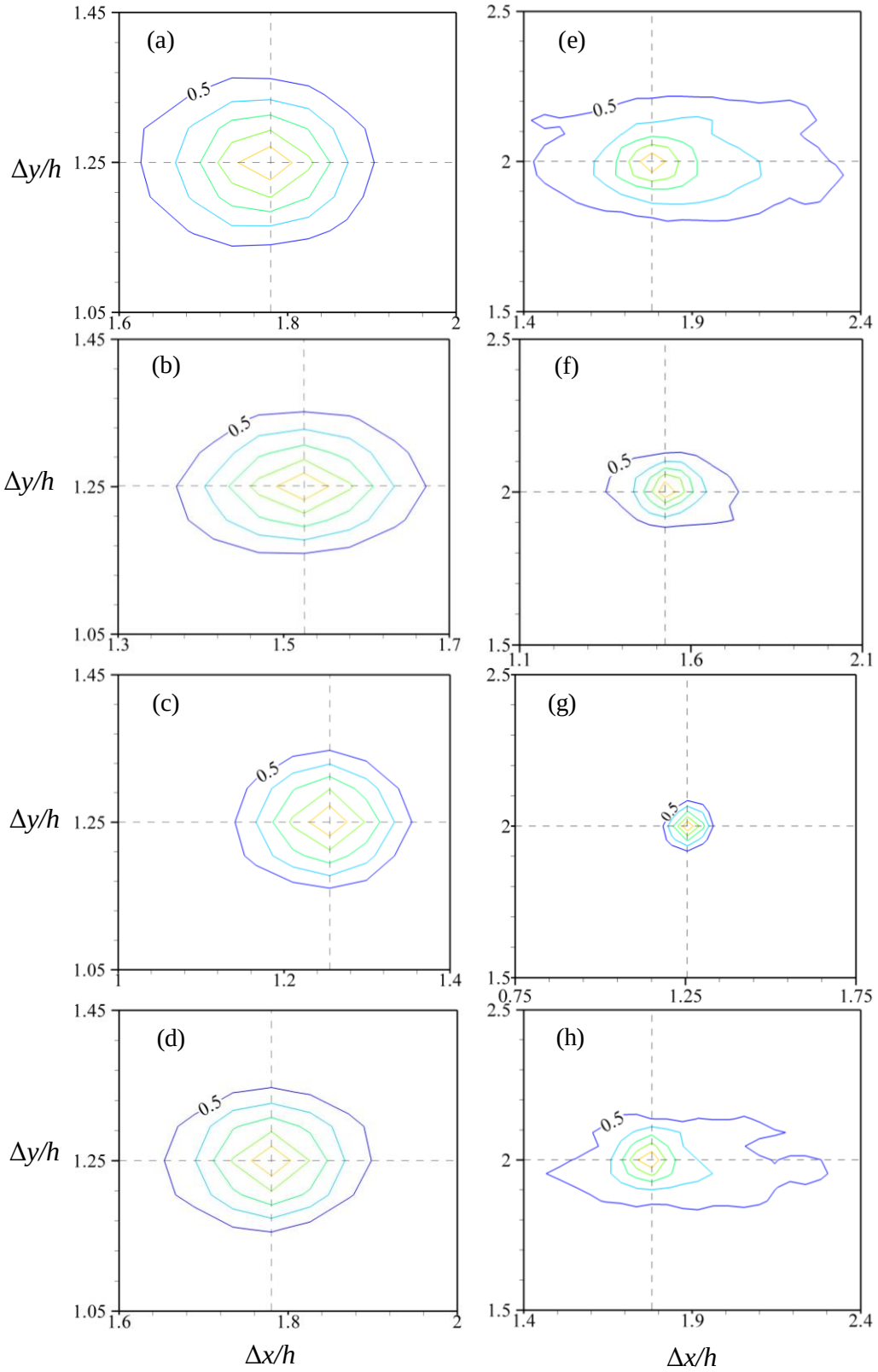

Figure 4.15: Contour plots of R_{uu} centered at x/h = 1 and y/h = 1.25 over (a) SM-SM, (b) SP-SM, (c) SG-SM and (d) SP-SP and y/h = 2 over (e) SM-SM, (f) SP-SM, (g) SG-SM and (h) SP-SP.

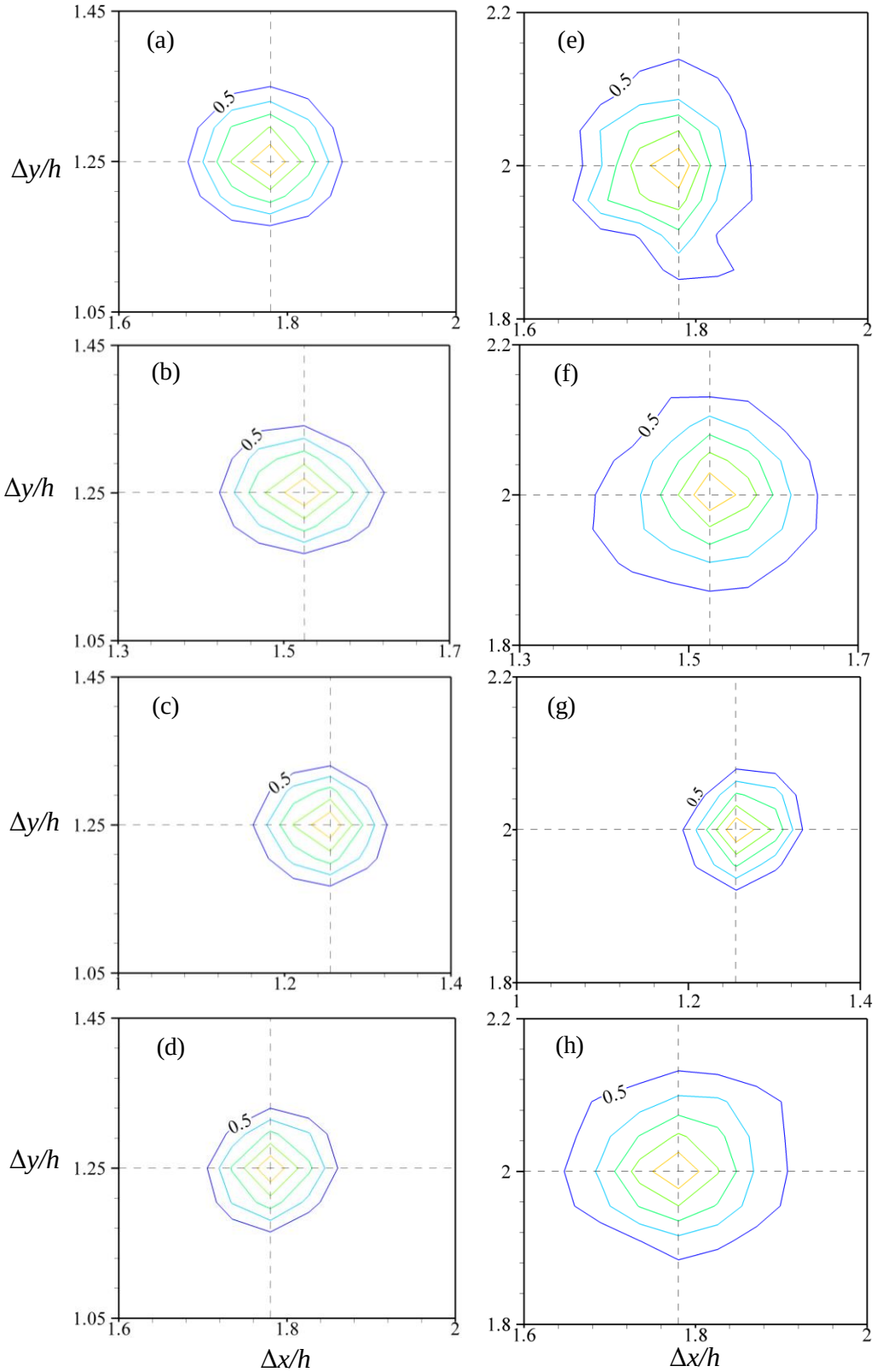

Figure 4.16: Contour plots of R_{vv} centered at x/h = 1 and y/h = 1.25 over (a) SM-SM, (b) SP-SM, (c) SG-SM and (d) SP-SP and y/h = 2 over (e) SM-SM, (f) SP-SM, (g) SG-SM and (h) SP-SP.

rounded and smaller in size compared to R_{uu} contours. The sizes of both R_{uu} and R_{vv} contours increased from y/h = 1.25 to y/h = 2, except for the case of SG-SM.

In the early recovery region (x/h = 5), Figure 4.17 and 4.18 show that the R_{uu} structures are still elongated in the streamwise direction and the R_{vv} structures are round. No significant roughness effect was observed in the R_{vv} contours. Figure 4.19 and 4.20 show the contour plots of R_{uu} and R_{vv} respectively centered at x/h = 60 and y/h = 1.25 and 2. Near the wall, the R_{uu} contours are elliptical in shape and elongated in the streamwise direction and R_{vv} contours are round. The extent of R_{uu} contours for SP-SM in the streamwise direction is about 6% larger compared to that of SM-SM. The smaller and compact sizes of the contours are consistent with the suppression of the wall-normal velocities associated with large scale motion in wall boundary layer (Volino et al., 2007; Wu and Christensen, 2010).

In comparison to the inner boundary layer, the outer layer showed a stronger spatial coherence. The shapes of the R_{uu} contours in Figure 4.15 are elliptical and the size is increased for all the cases which was also observed by Essel and Tachie, 2015 in the recovery region. The SP-SM and SP-SP cases are still showing stronger correlation in the streamwise distance compared to the other two cases.

The integral length scales were determined using the one dimensional profiles obtained along the vertical dashed line passing through the self-correlation point. The distribution of integral length scales from the early redevelopment region to the far recovery region is shown in Figure 4.21 at selected streamwise locations (x/h = 5, 20 and 60). The L_y^u was estimated as the area under the $R_{uu}(y)$ curve from the self-correlation point to the point

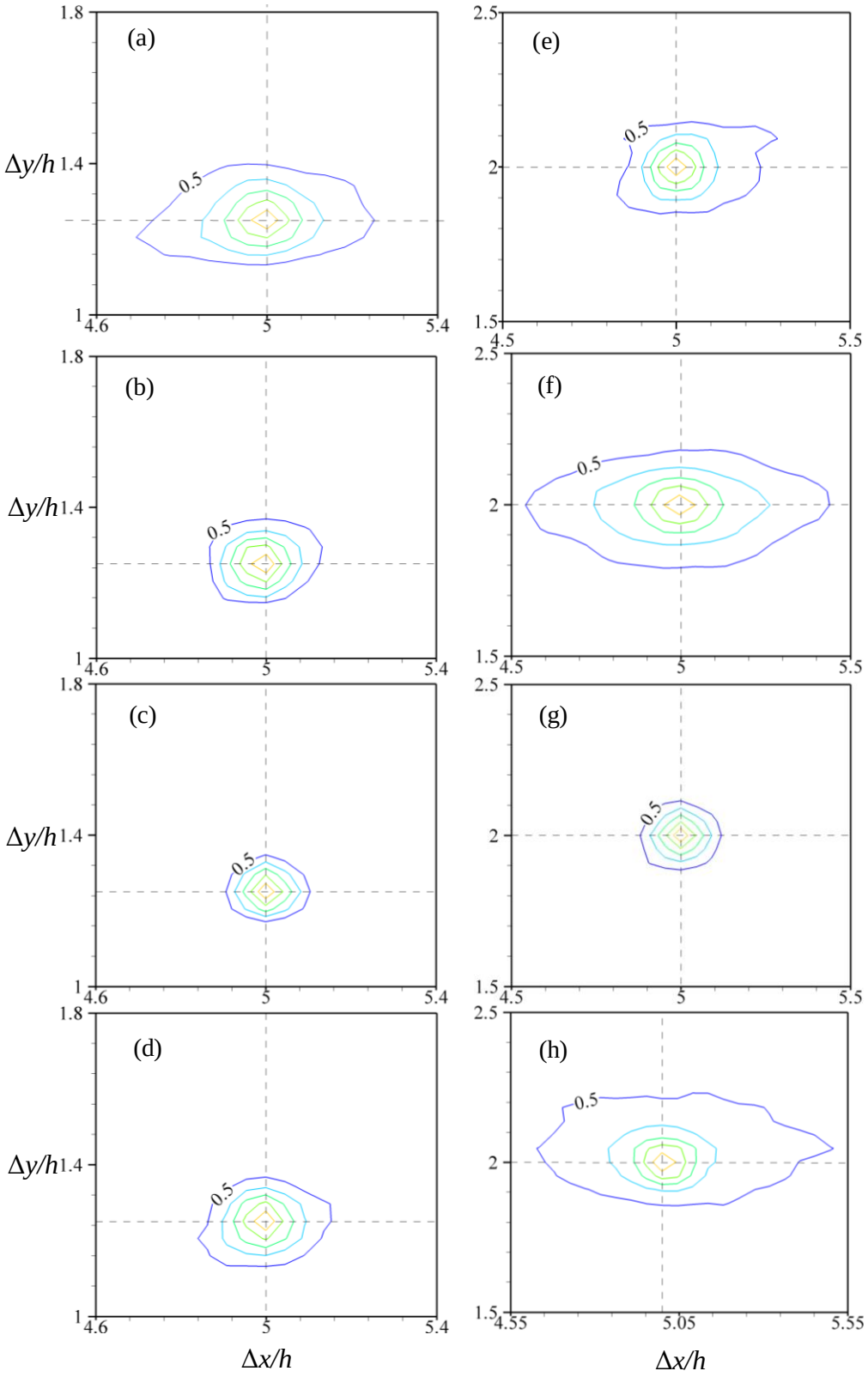

Figure 4.17: Contour plots of R_{uu} centered at x/h = 5 and y/h = 1.25 over (a) SM-SM, (b) SP-SM, (c) SG-SM and (d) SP-SP and y/h = 2 over (e) SM-SM, (f) SP-SM, (g) SG-SM and (h) SP-SP.

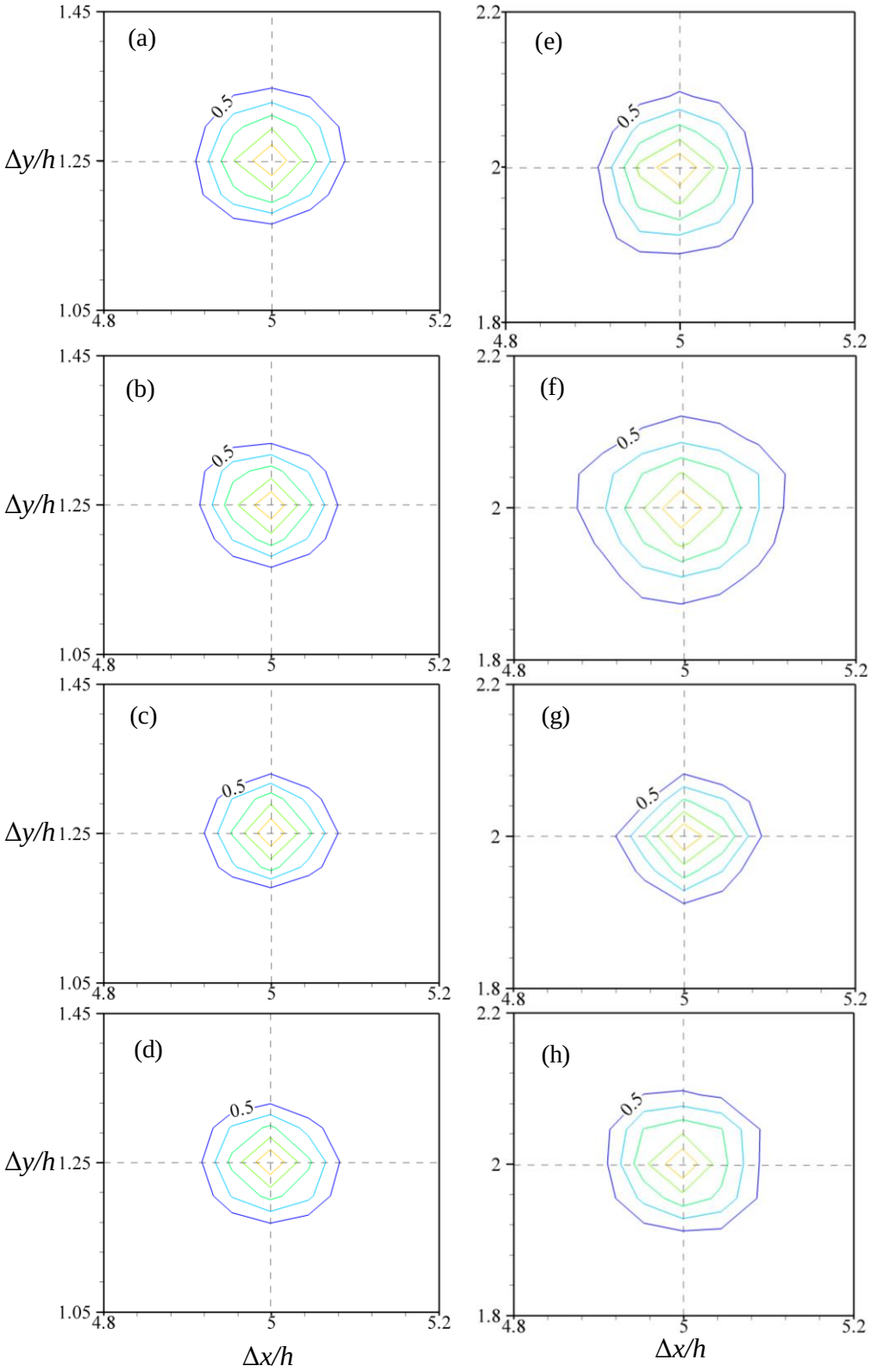

Figure 4.18: Contour plots of R_{vv} centered at x/h = 5 and y/h = 1.25 over (a) SM-SM, (b) SP-SM, (c) SG-SM and (d) SP-SP and y/h = 2 over (e) SM-SM, (f) SP-SM, (g) SG-SM and (h) SP-SP.

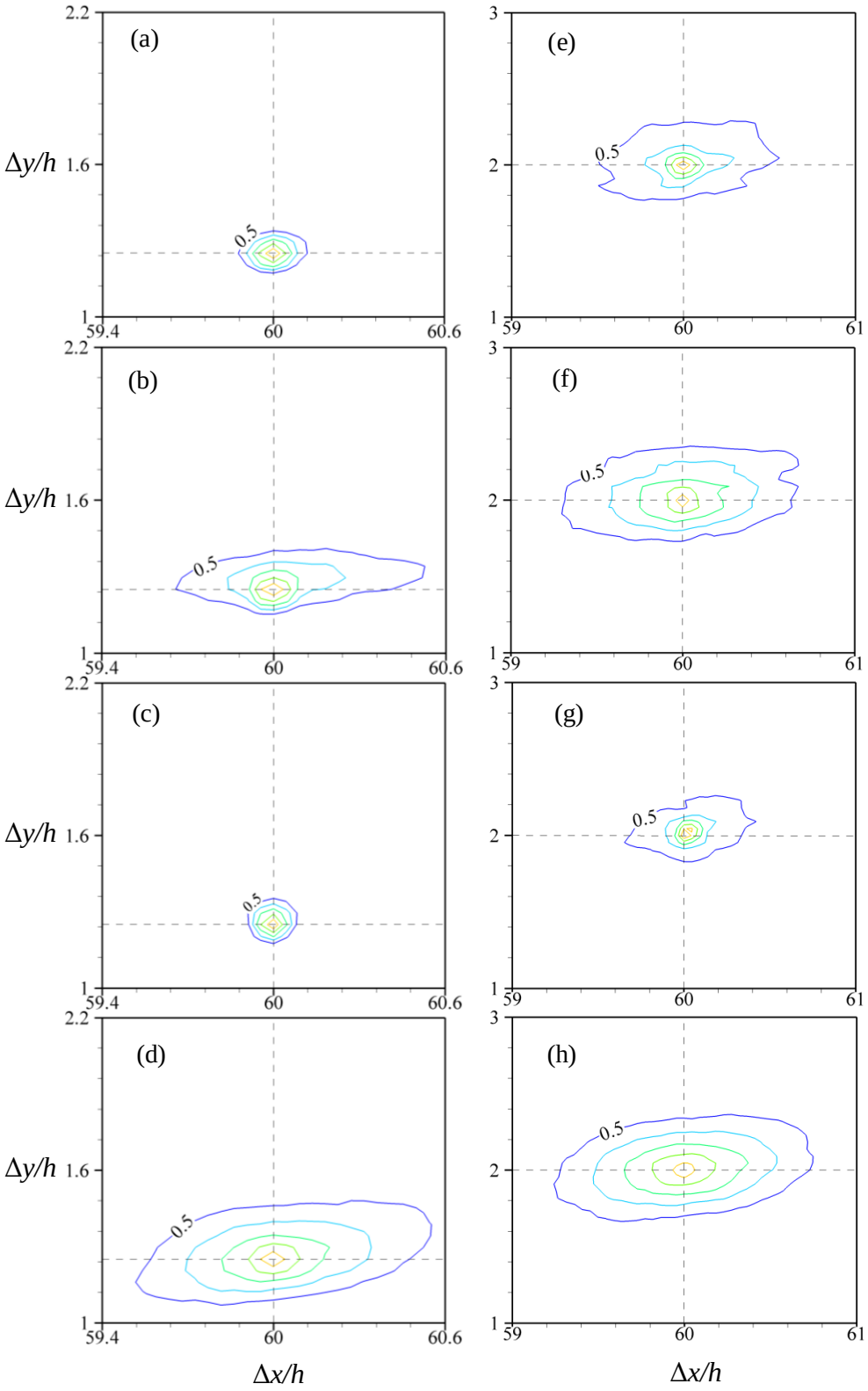

Figure 4.19: Contour plots of R_{uu} centered at x/h = 60 and y/h = 1.25 over (a) SM-SM, (b) SP-SM, (c) SG-SM and (d) SP-SP and y/h = 2 over (e) SM-SM, (f) SP-SM, (g) SG-SM and (h) SP-SP.

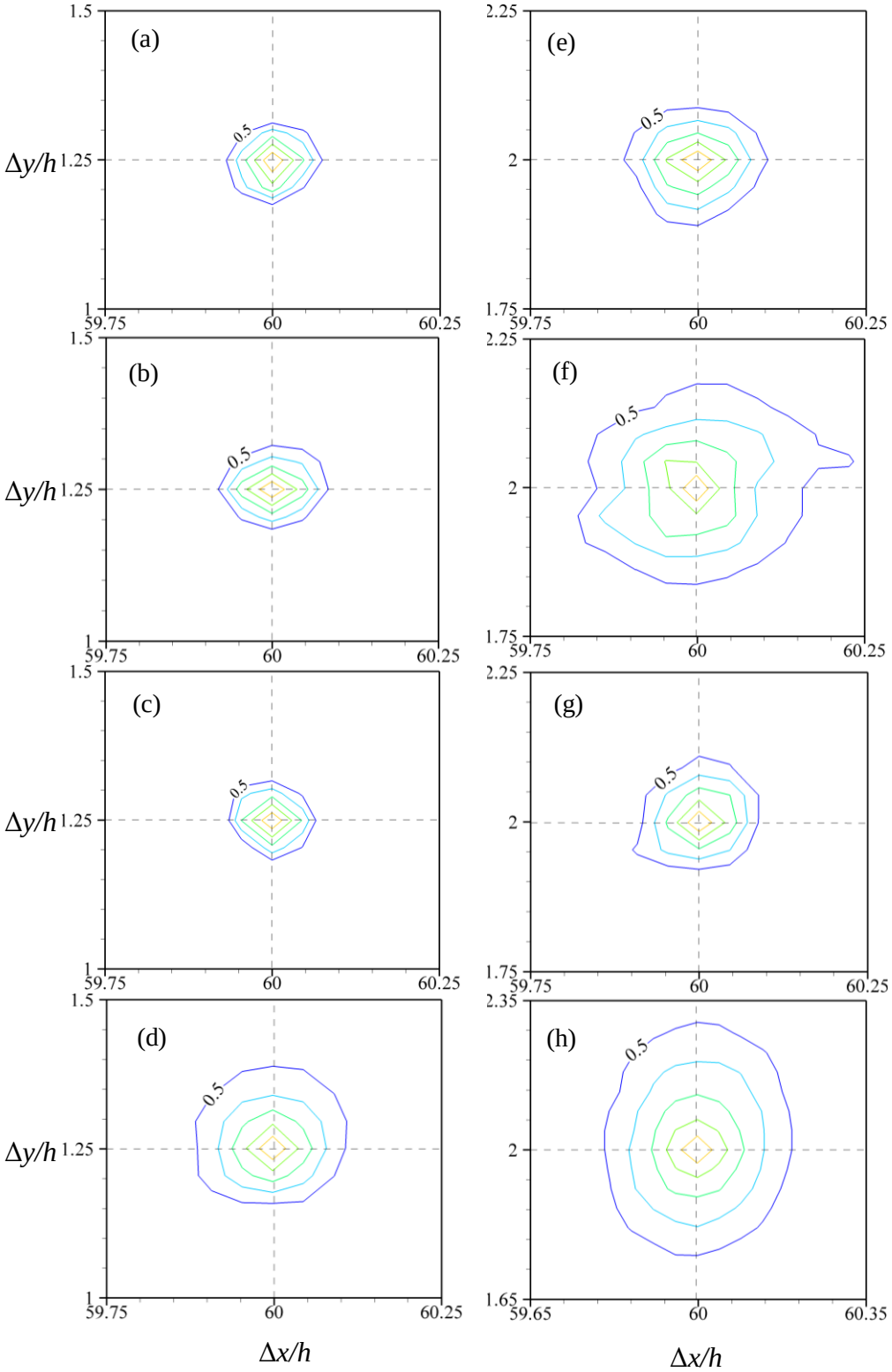

Figure 4.20: Contour plots of R_{vv} centered at x/h = 60 and y/h = 1.25 over (a) SM-SM, (b) SP-SM, (c) SG-SM and (d) SP-SP and y/h = 2 over (e) SM-SM, (f) SP-SM, (g) SG-SM and (h) SP-SP.

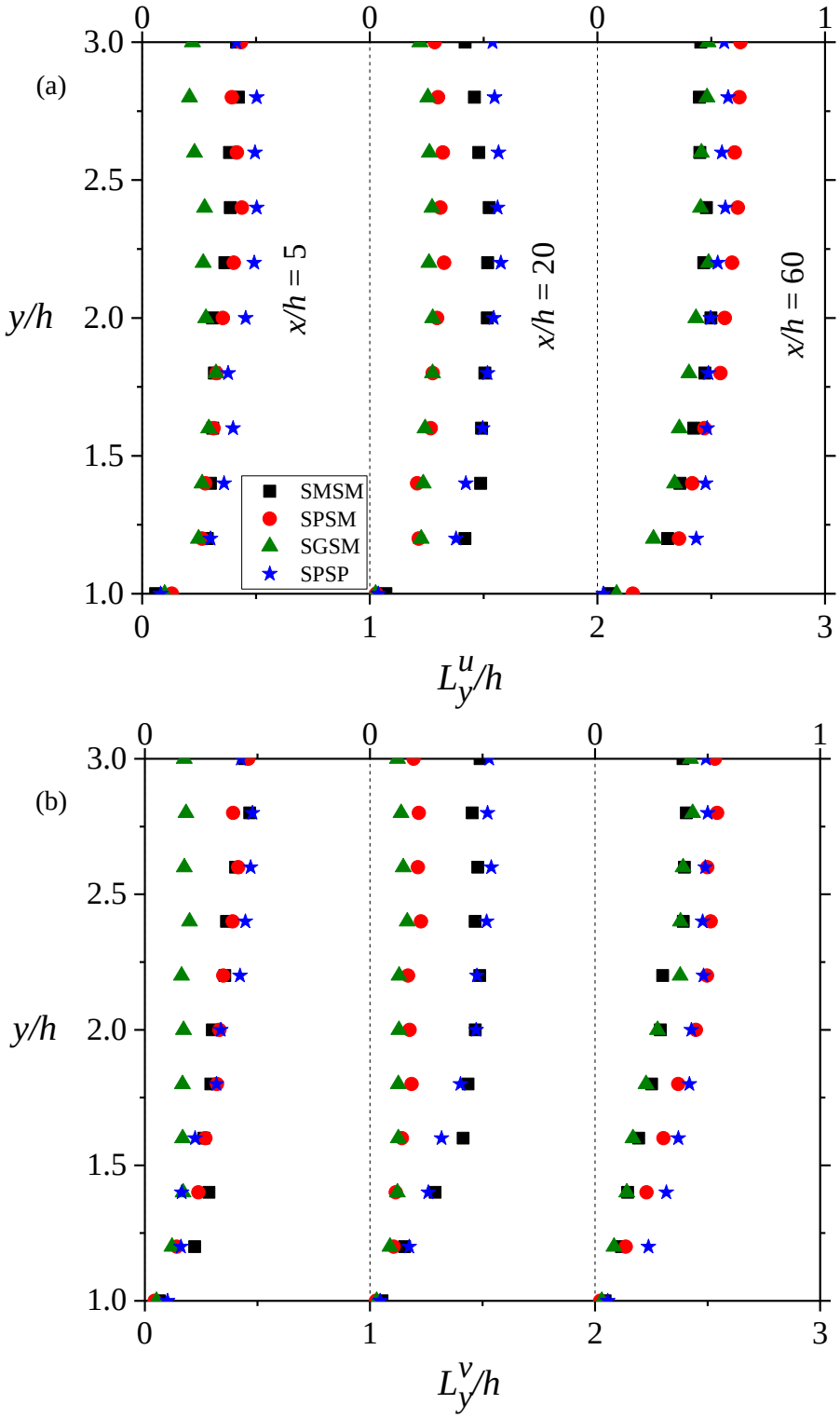

Figure 4.21 Distribution of integral length scales at selected streamwise locations in the recovery region.

where the curve goes to zero. Similarly, the L_y^v was estimated as the area under the $R_{vv}(y)$ curve from the self-correlation point to the point where the curve goes through zero. It is evident from Figure 4.21 that the L_y^u and L_y^v increase gradually from the step wall up to y/h = 2 and remain constant after that. The upstream roughness (SP-SM and SG-SM) decreases the integral length scales in the early recovery regions but in the later stage of the recovery, the SP-SM and SP-SP showed higher values of L_y^u and L_y^v. For example, at x/h = 20, the peak value of L_y^u of SM-SM is 38% higher than the peak value of SP-SM but at x/h = 60, the peak value of L_y^u of SM-SM is 17% lower than that of SP-SM. Similar observations were also made for L_y^v peak values. This dissimilarity is qualitatively similar to the observations made from Figure 4.19 and 4.20. On the contrary, the integral length scales for the SP-SP case were consistently higher from the early recovery all the way to the last measurement position. This indicates that although the upstream wall roughness decreased the size of the large scale structures in the early recovery region, the downstream wall roughness has a stronger spatial coherence in the streamwise and wall-normal velocity fluctuations which persists throughout the recovery region.

4.4 Quadrant analysis

Quadrant hole analysis was also performed in the recirculation region to evaluate the impact of wall roughness on the dominant Reynolds shear stress event. The Reynolds shear stress can be decomposed into contributions from four quadrant events following the methodology described by Lu and Williamarth, 1973, Quadrant 1: outward interactions ($Q1$), Quadrant 2: ejections ($Q2$), Quadrant 3: inward interactions ($Q3$) and Quadrant 4: sweeps ($Q4$).

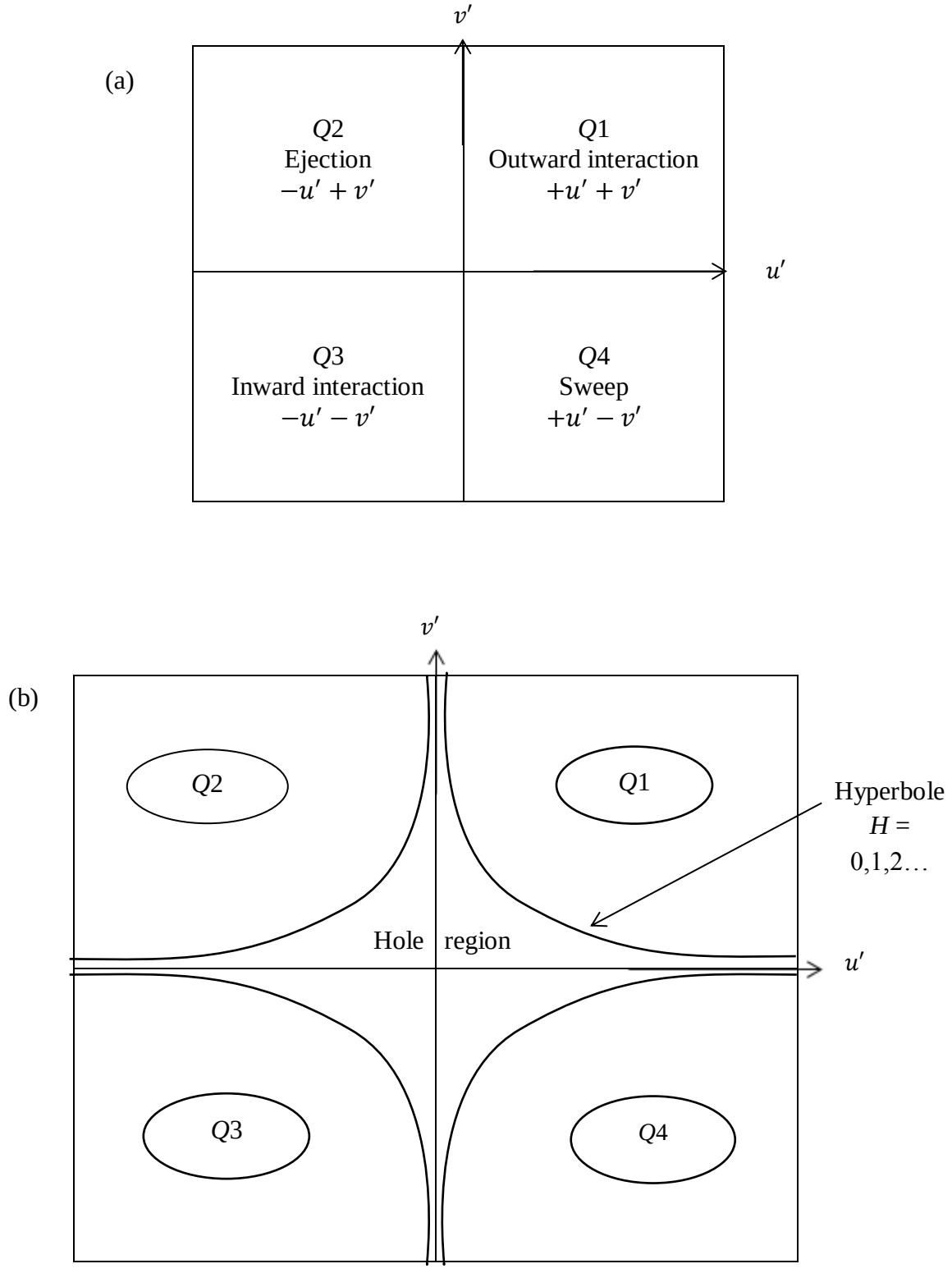

Figure 4.22 (a) Quadrant decomposition of the fluctuating components of velocity, (b) Illustration of quadrant hole analysis technique with the four quadrants and hole region.

According to Nolan et al., 2010, quadrant hole analysis is the method to measure the extent of contributions to the Reynolds shear stress in each quadrant by limiting the data to consider values above a threshold value. This threshold value defines the hole region *H* when applied to each quadrant and as a result, the data from that region is removed. The hole region can be enlarged by increasing the value of *H* in order to determine the contribution of the remaining data outside the hole. The quadrant hole analysis technique is illustrated in Figure 4.22 (a) and (b). The equation used to fragment the contributions from four different quadrants across the whole PIV field of view by excluding the data outside of a hyperbolic hole size of *H* is as follows

$$\overline{u'v'}(x) = \frac{1}{N}\sum_{j=1}^{N} u'(x)v'(x)I_Q(x) \tag{5}$$

where *N* is the number of total PIV sample size and I_Q is the indicator function which is defined as

$$I_Q(x) = \begin{cases} 1, & \text{when } \left|u'(x), v'(x)\right|_Q \geq H\left|u'v'\right|_{\max} \\ 0, & \text{otherwise} \end{cases} \tag{6}$$

where $|u'v'|_{\max}$ is the maximum value of the mean Reynolds shear stress in a particular case. In this study, only hole size $H = 0$ was used to examine the contributions to the shear stress from all events in order to better understand the effects of wall roughness on the Reynolds shear stress. Each quadrant event occupies a certain space in the flow and the space fraction occupied by each quadrant event is given by

$$N_Q(x) = \frac{\sum I_Q(x)}{N} \tag{7}$$

where N_Q is the space fraction.

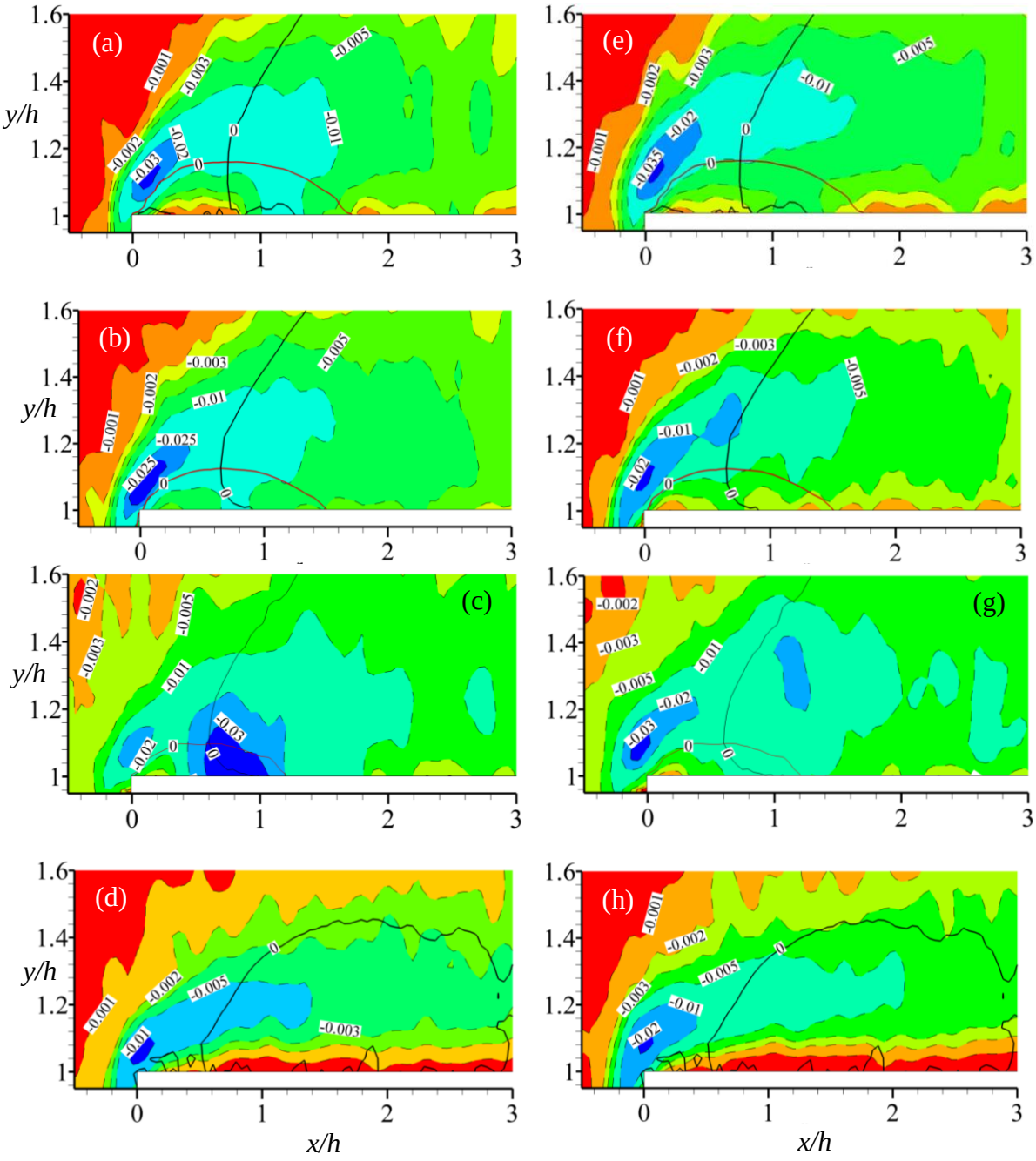

Figure 4.23 Contour plots of contributions from *Q*1 events for (a) SM-SM, (b) SP-SM, (c) SG-SM and (d) SP-SP and *Q*3 events for (e) SM-SM, (f) SP-SM, (g) SG-SM and (h) SP-SP.

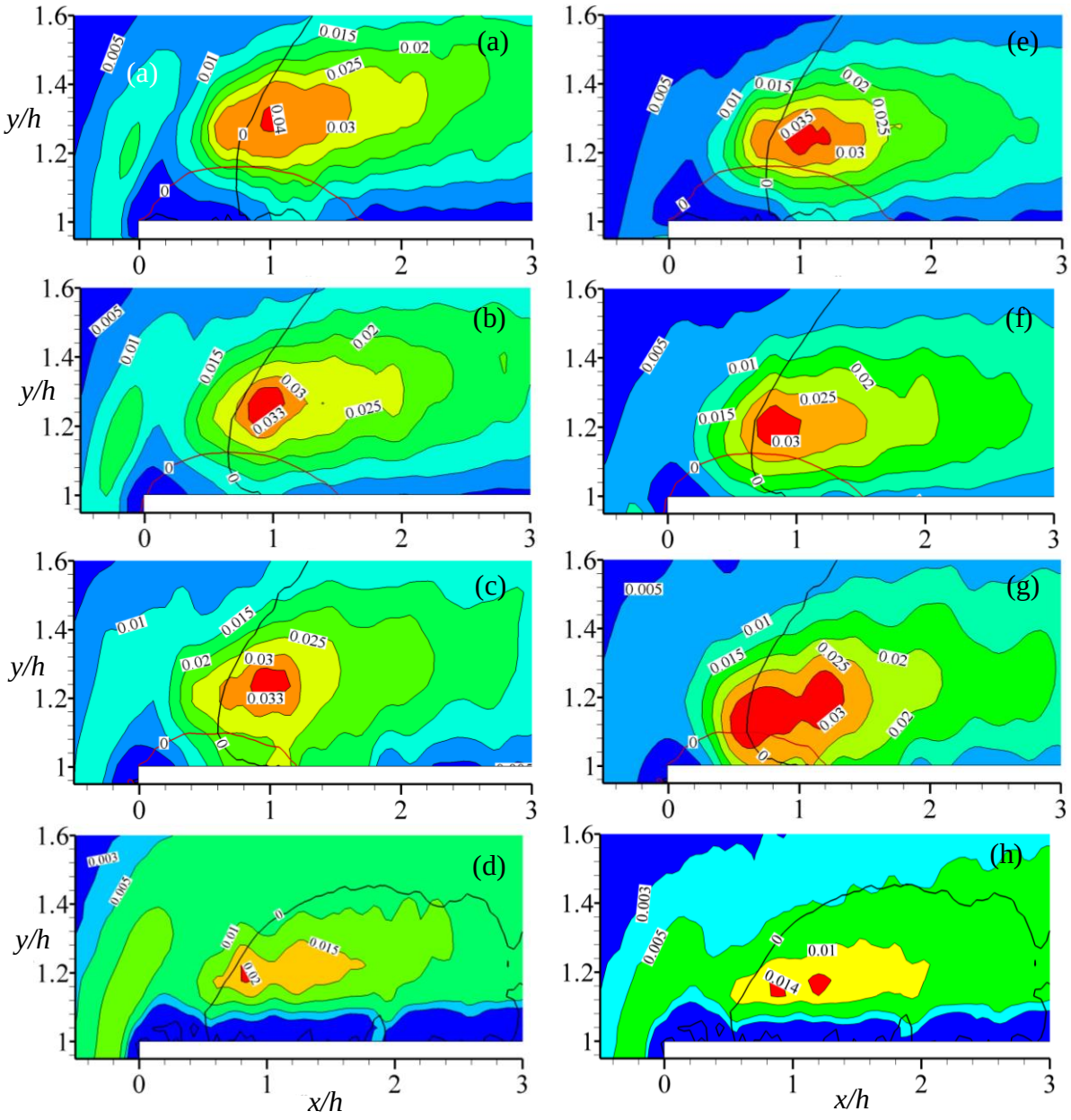

Figure 4.24 Contour plots of contributions from *Q*2 events for (a) SM-SM, (b) SP-SM, (c) SG-SM and (d) SP-SP and *Q*4 events for (e) SM-SM, (f) SP-SM, (g) SG-SM and (h) SP-SP.

Figure 4.23 (a, b, c, d) and (e, f, g, h) represents the contour plots of contributions of outward interactions ($Q1$ events) and inward interactions ($Q3$ events) respectively, while Figure 4.24 (a, b, c, d) and (e, f, g, h) represents contour plots of the ejections ($Q2$ events) and sweeps ($Q4$ events) respectively for a threshold value of $H = 0$. This analysis was performed over smooth and rough walls in P0 and P1 measurement planes ($-4.7 \leq x/h \leq 4.3$). The $U = 0$ and $V = 0$ lines are imposed on each contour which are represented by red and black colour respectively. The $U = 0$ line symbolizes the size of the recirculation region (as mentioned in Section 4.2.1) and the $V = 0$ line represents the upward transport of low momentum fluid and downward transport of high momentum fluid before and after the line respectively (as mentioned in Section 4.2.4). Near the leading edge of the step shown in Figure 4.23, both $Q1$ and $Q3$ events contribute significantly to the negative $-u'v'$, although the contribution varied depending on wall roughness. For example, the peak value of $Q3$ for SM-SM was 17% larger than corresponding $Q1$ value and the peak value of $Q1$ for SP-SM was 25% larger than corresponding value of $Q3$. In terms of wall roughness, changing the wall from smooth to rough decreased the contributions from both $Q1$ and $Q3$ events.

In the present study, majority of the positive $-\overline{u'v'}$ after one step height from the leading edge of the step was contributed by ejections and sweeps which is in a good agreement with the previous studies (Ren and Wu, 2011; Hattori and Nagano, 2010). However, near the reattachment, the contributions of ejections were higher than sweeps. For example, the values of $Q2$ for SM-SM, SP-SM, SG-SM and SP-SP were 14%, 10%, 10% and 43% higher respectively than the corresponding peak values of $Q4$. On the other hand, in the

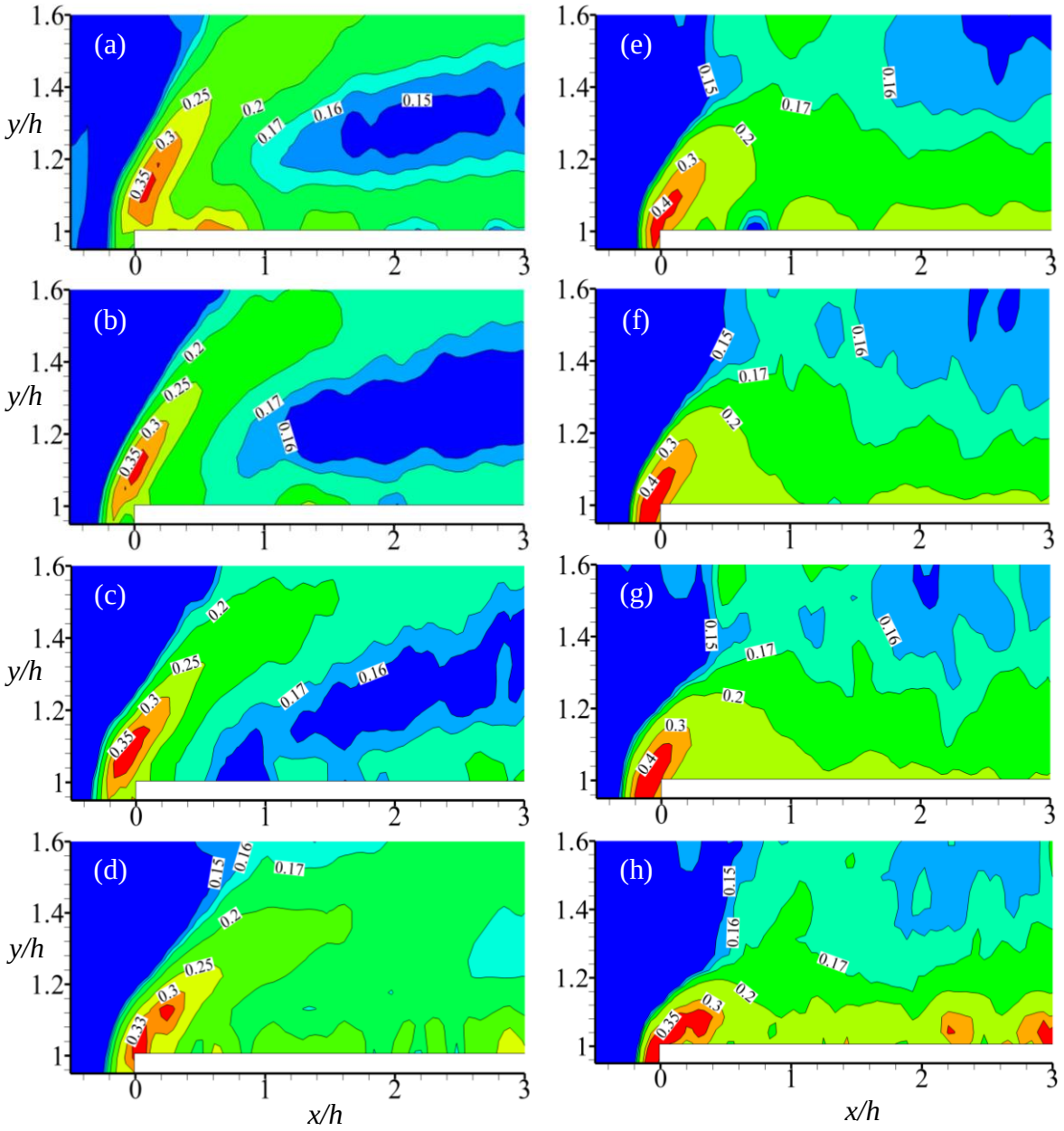

Figure 4.25 Contour plots of space fractions occupied by *Q*1 events (a) SM-SM, (b) SP-SM, (c) SG-SM and (d) SP-SP and *Q*3 events (e) SM-SM, (f) SP-SM, (g) SG-SM and (h) SP-SP.

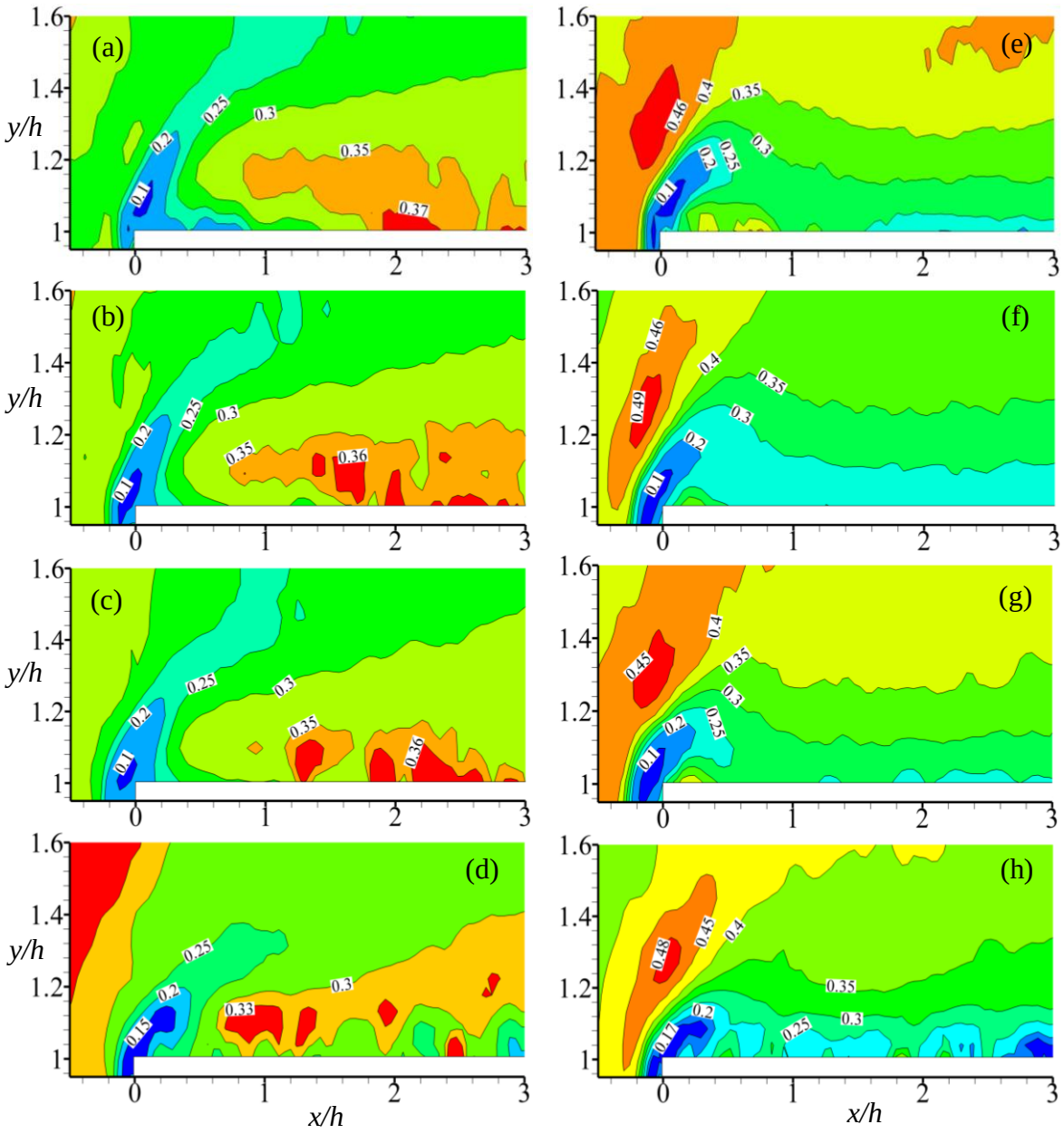

Figure 4.26 Contour plots of space fractions occupied by *Q*2 events (a) SM-SM, (b) SP-SM, (c) SG-SM and (d) SP-SP and *Q*4 events (e) SM-SM, (f) SP-SM, (g) SG-SM and (h) SP-SP.

immediate vicinity of the leading edge of the step $Q1$ and $Q3$ were the major contributors. It is shown in Figure 4.24 that wall roughness reduced the contributions of both ejections and sweeps. SP-SP decreased the peak values of $Q2$ and $Q4$ by as much as 50% and 60% respectively compared to the corresponding values of SM-SM.

The space fractions occupied by outward and inward interactions are shown in Figure 4.25 and ejections and sweeps are shown in Figure 4.26. The space fractions are qualitatively similar for the different roughness topologies. In the vicinity of the leading edge of the step, $Q3$ events occupy around 40% of the space which is higher than approximately 35% occupied by $Q1$. Upstream wall roughness has no significant effect but downstream wall roughness decreased the $Q1$ and $Q3$ space fraction by 5% and 12% respectively. In the region immediately downstream of the step, both Q1 and Q3 occupy around 34% of the space meaning $Q2$ and $Q4$ occupy around 66%. Figure 4.26 shows that the maximum space fraction occupied by $Q2$ is 37% whereas for $Q4$ it is 49%. Occurrence of ejections is closer to the step while the sweeps occupy more space further away from the wall. Wall roughness decreased the ejection event's space occupancy by approximately 10% but increased the sweep's space occupancy by approximately 7%. It should be noted that, although the peak value of $Q2$ and $Q4$ events was observed at around $x/h = 1$ (Figure 4.24), the maximum space fraction occupied by $Q2$ and $Q4$ was observed at the leading edge at around $y/h = 1.3$. This phenomenon can be explained by the fact that although the peak values occurred at $x/h = 1$, the frequency of the signal i.e. the frequency of the occurrence of events was higher at the leading edge at $y/h = 1.3$.

CHAPTER 5

SUMMARY, CONCLUSIONS AND FUTURE WORK

5.1 Summary

An experimental study was performed to investigate the effects of wall roughness on the reattachment and recovery regions over a forward facing step in an open channel turbulent flow. The experiments were undertaken over a smooth upstream and downstream wall, an upstream rough wall produced from sandpaper 36 grit and a smooth downstream wall, an upstream rough wall produced from sand grain and a smooth downstream wall, and an upstream rough wall coated with sandpaper 36 grit and a rough downstream wall coated with sandpaper 36 grit. A particle image velocimetry technique was used to perform the velocity measurements up to 60 step heights downstream. The flow was analyzed using mean velocities, Reynolds stresses, turbulent kinetic energy, integral parameters and some of the budget terms in the turbulent kinetic energy transport equation. Two point correlation coefficients and quadrant analysis were also used to investigate the impact of wall roughness on the large scale coherent structures in the flow.

5.2 Conclusions

The major conclusions from this study are summarized below

- Wall roughness decreased the reattachment length over SP-SM and SG-SM by 14% and 29%, respectively, compared with corresponding value over the reference smooth wall. SP-SP did not show any distinct recirculation bubble.

- In the recirculation region, wall roughness reduced the peak values of both the streamwise and wall-normal mean velocities. Further downstream of reattachment, the streamwise mean velocity were independent of upstream wall roughness (SP-SM, SG-SM); however the downstream wall roughness (SP-SP) reduced the level of streamwise mean velocity which is an artifact of the rough wall turbulent boundary layer.

- Wall roughness enhanced the levels of streamwise and wall-normal Reynolds normal stresses in the recirculation region, but the Reynolds shear stresses were nearly independent. The results also show that the Reynolds stresses require longer streamwise distance to completely collapse on to the upstream profiles than required for the mean velocity.

- The results from the mean velocity and integral parameters showed that the inner and outer layers of the boundary layer downstream of the reattachment recover reasonably well at x/h = 40 irrespective of the upstream and downstream wall conditions.

- Wall roughness suppressed the production of turbulent kinetic energy in the recirculation region. However, no significant wall roughness effect was observed on TKE in the recovery region.

- The investigation of integral length scales form two-point autocorrelation function revealed that the upstream wall roughness decreased the size of the large scale structures in the early recovery region; however, the downstream wall roughness has a stronger spatial coherence in the streamwise and wall-normal velocity fluctuations which persists throughout the recovery region.

- Quadrant analysis revealed that wall roughness reduced the contributions of both ejections and sweeps; however, near the reattachment, the contributions of ejections were higher than sweeps.

5.3 Future work

The universality of the present findings can be confirmed by conducting velocity measurements over various types of roughness elements. It is recommended that future work should measure the third velocity component using a stereo-PIV in order to obtain a complete description of flow dynamics. Also, the results can be used in numerical simulation to model real life problems.

REFERENCES

Adams, E., Johnston, J., 1988. Flow structure in the near-wall zone of a turbulent separated flow. AIAA J. 26, 932-939.

Afzal, B., Faruque, M.A., Balachandar, R., 2010. Effect of Reynolds number, near-wall perturbation and turbulence on smooth open-channel flows. J. Hydraulic Research. 47, 66-81.

Ampadu-Mintah, A., Tachie, M.F., 2015. Surface roughness effects on separated and reattached turbulent flow in open channel. J. Hydraulic Research. 53, issue-3

Awasthi, M., Lowe, K.T., Glegg, S.A.L, 2012. High Reynolds Number Turbulent Boundary Layer Flow over Small Forward Facing Steps. 17th AIAA/CEAS Aeroacoustics Conference, Portland, Oregon, 2012.

Balachandar, R., Tachie, M.F., 2001. A study of boundary layer-wake interaction in shallow open channel flows. Exp. In Fluids. 30, 511-521.

Barri1, M.G., El Khoury, K., Andersson H.I., Pettersen, B., 2010. DNS of backward-facing step flow with fully turbulent inflow. Int. J. Numerical Methods in Fluids. 64, 777–792.

Bergeles, G., Athanassiadis, N., 1983. The flow past a surface-mounted obstacle. J. Fluids Eng. 105, 461–463.

Bradshaw, P., Wong, F., 1972. The reattachment and relaxation of a turbulent shear layer. J. Fluid Mech. 52, 113–135.

Casarsa, L., Giannattasio, P., 2008. Three-dimensional features of the turbulent flow through a planar sudden expansion. Phys. Fluids. 20, 015103.

Castro, I.P., Epik, E., 1996. Boundary-layer relaxation after a separated region. Exp. Thermal Fluid Sci. 13, 338-348.

Castro, I.P., Epik, E., 1998. Boundary layer development after a separated region. J. Fluid Mech. 374, 91-116.

Coles, D., 1956. The Law of the Wake in the Turbulent Boundary Layer. J. Fluid Mech., 1, 191–226.

De Brederode, V., Bradshaw, P., 1972. Three-dimensional flow in nominally two-dimensional separation bubbles: flow behind a rearward-facing step. Imp. Coll. Aeronaut. Rep. 72–19.

Driver, D.M., Seegmiller, H.L., Marvin, J.G., 1987. Time-dependent behavior of a reattaching shear layer. AIAA J. 25, 914–919.

Essel, E.E., Tachie, M.F., 2015. Upstream roughness and Reynolds number effects on turbulent flow structure over forward facing step. Int. J. Heat Fluid Flow. 2015.11.004

Essel, E.E., Tachie, Nematollahi, A., Thacher, E.W., Tachie, M.F., 2015. Effects of upstream roughness and Reynolds number on separated reattached turbulent flow. J. Turbul. 16, 872-899.

Fernholz, H.H., Finley, P.J., 1996. The incompressible zero-pressure-gradient turbulent boundary layer: an assessment of the data. Aerospace Sci. 32, 245-311.

Flack, K.A., Schultz, M.P., 2010. Review of Hydraulic Roughness Scales in the Fully Rough Regime. J. Fluids Eng. 132, 041203–10.

Forliti, D.J., Strykowski, P.J., Debatin, K., 2000. Bias and precision errors of digital particle image velocimetry. Exp. Fluids 28, 436–447.

H. Hattori and Y. Nagano, 2010. Investigation of turbulent boundary layer over forward-facing step via direct numerical simulation. Int. J. Heat Fluid Flow. 31, 284–294.

Johansson, A., Alfredsson, P., 1983. Effects of imperfect spatial resolution on measurements of wall-bounded turbulent shear flows. J. Fluid Mech. 137, 409–421.

Jovic, S., 1996. An experimental study of a separated/reattached flow behind a backward-facing step; Re (sub h) = 37, 000, NASA Tech. Memor.

Kim, B.N., Chung, M.K., 1995. Experimental study of roughness effects on the separated flow over a backward-facing step. AIAA J. 33, 159–160.

Kiya, M., Sasaki, K., 1983. Structure of a turbulent separation bubble. J. Fluid Mech. 137, 83-113.

Krogstad, P., Antonia, R., 1994. Structure of turbulent boundary layers on smooth and rough walls. J. Fluid Mech. 277, 1–21.

Krogstad, P.A., Antonia, R.A., Browne, L.W., 1992. Comparison between rough and smoothwall turbulent boundary layers. J. Fluid Mech. 245, 599–617.

Largeau, J.F., Moriniere, V., 2007. Surface pressure fluctuations and topology in separated flows over a forward-facing Step. Exp. Fluids. 42, 21–40.

Lu, S.S., Willmarth, W.W., 1973. Measurement of the structure of the Reynolds stress in a turbulent boundary layer, J. Fluid Mech., 60, 481–511.

Mei, M., Adrian, R.J., Hanratty, T.J., 1991. Particle dispersion in isotropic turbulence under stokes drag and Basset force with gravitational settling. J. Fluid Mech. 225, 481-495.

Nolan, K.P., Walsh, E.J., Mceligot, D.M., 2010. Quadrant analysis of a transitional boundary layer subject to free-stream turbulence. J. Fluid Mech. 658, 310-335

Piirto, M., Saarenrinne, P., Eloranta, H., Karvinen, R., 2003. Measuring turbulence energy with PIV in a backward-facing step flow. Exp. Fluids 35, 219–236.

Prasad, A., Adrian, R., Landreth, C., Offutt, P., 1992. Effect of resolution on the speed and accuracy of particle image velocimetry interrogation. Exp. Fluids 116, 105–116.

Purtell. L.P., Klebanoff, P.S., Buckley, F.T., 1981. Turbulent boundary layer at low Reynolds number. Phys. Fluids, 24, 802–811.

Raffel, M., Willert, C.E., Kompenhaus, J., 1998. Particle Image Velocimetry: A Practical Guide. Springer Verlag.

Ren, H., Wu, Y., 2011. Turbulent boundary layers over smooth and rough forward-facing steps. Phys. Fluids. 23, 045102.

Schlichting, H., Kestin, J., 1979. Boundary-layer Theory. Mcgraw-Hill, New York.

Shao, W., Agelin-chaab, M., 2016. Turbulent flows over forward facing steps with surface roughness. J. Fluids Eng. Vol. 138/021103-1

Sherry, M., Jacono, D.Lo., Sheridan, J., 2010. An experimental investigation of the recirculation zone formed downstream of a forward facing step. J. Wind Eng. Ind. Aerodyn. 98(12), 888–894.

Smits, A.J., 1983. Scaling parameters for a time-averaged separation bubble. J. Fluids Eng. 104, 178-184.

Tachie, M.F., Balachandar, R., Bergstrom, D.J., 2001. Open channel boundary layer relaxation behind a forward facing step at low Reynolds number. J. Fluids Eng. 123, 539-544.

Tachie, M.F., Bergstrom, D.J., Balachandar, R., 2000. Rough surface turbulent boundary layers in shallow open channel flow. J. Fluids Eng. 122, 533–541.

Tachie, M.F., Bergstrom, D.J., Balachandar, R., 2003. Roughness effects in low- Re_τ open-channel turbulent boundary layers. Exp. Fluids, 35, 338–346.

Volino, R.J., Schultz, M.P., Flack, K.A., 2007. Turbulence structure in rough- and smooth-surface boundary layers. J. Fluid. Mech. 592, 263-293.

Westphal, R. V., Johnston, J.P., Eaton, J.K., 1984. Experimental study of flow reattachment in a single-sided sudden expansion. PHD Thesis, Mechanical Engineering Department, Stanford University.

Wu, Y., Christensen, K.T., 2010. Spatial structure of a turbulent boundary layer with irregular surface roughness. J. Fluid Mech. 655, 380-418.

Wu, Y., Ren, H., 2013. On the impacts of coarse-scale models of realistic roughness on a forward-facing step turbulent flow. Int. J. Heat Fluid Flow. 40, 15–31.